CURRICULUM VITAE

Jennifer Megan Canono Mariano

Doctor of Philosophy, Fall 2024
Department of Biochemistry and Molecular Biology
University of Maryland School of Medicine
mariano.jmc2@gmail.com

EDUCATION

2018-2024	Ph.D. Candidate, Graduate Program in Biochemistry and Molecular Biology University of Maryland School of Medicine, Baltimore, MD, USA Advisor: Aikaterini Kontrogianni-Konstantopoulos, Ph.D.
2011-2015	Bachelor of Science, Dept. of Chemistry, Dept. of Biology Loyola University Maryland, Baltimore, MD, USA

PUBLICATIONS

1. Iyer A, Lauerova B, **Mariano J**, Haberlová J, Lassuthova P, Zidkova J, Wright NT, Kontrogianni-Konstantopoulos A. Compound heterozygous variants in MYBPC1 lead to severe distal arthrogryposis type-1 manifestations. Gene. 2024 Jun 5;910:148339. doi: 10.1016/j.gene.2024.148339. Epub 2024 Mar 2. PMID: 38438057; PMCID: PMC10981553.

2. Ranu N, Laitila J, Dugdale HF, **Mariano J**, Kolb JS, Wallgren-Pettersson C, Witting N, Vissing J, Vilchez JJ, Fiorillo C, Zanoteli E, Auranen M, Jokela M, Tasca G, Claeys KG, Voermans NC, Palmio J, Huovinen S, Moggio M, Beck TN, Kontrogianni-Konstantopoulos A, Granzier H, Ochala J. NEB mutations disrupt the super-relaxed state of myosin and remodel the muscle metabolic proteome in nemaline myopathy. Acta Neuropathol Commun. 2022 Dec 17;10(1):185. doi: 10.1186/s40478-022-01491-9. PMID: 36528760; PMCID: PMC9758823.

3. Portney BA, Khatri R, Meltzer WA, **Mariano JM**, Zalzman M. ZSCAN4 is negatively regulated by the ubiquitin-proteasome system and the E3 ubiquitin ligase RNF20. BBRC. 2018 Mar 25;498(1):72-78.

CONFERENCE PRESENTATIONS

2024 May	2024 Myofilament Meeting Monona Terrace Community and Convention Center, Madison, WI Poster presentation: Sex-dependent progression of the *MYBPC1* E248K Myotrem myopathy in response to aging
2024 Apr	46th Annual UMB Graduate Research Conference University of Maryland School of Medicine, Baltimore, MD Oral presentation: Sex-Dependent Progression of the *MYBPC1* E248K Myotrem Myopathy in Response to Aging Award: GRC Outstanding Presentation Award
2024 Apr	The 28th Interdisciplinary Training Program in Muscle Biology Retreat University of Maryland School of Medicine, Baltimore, MD Poster presentation: Sex-dependent Progression of the *MYBPC1* E248K Myopathy with Tremor in Response to Aging
2024 Jan	Biochemistry and Molecular Biology Graduate Program in Life Science Retreat University of Maryland School of Medicine, Baltimore, MD Oral presentation: Sex-specific phenotypic characterization of *MYBPC1*-linked Myotrem myopathy in mid- and late adulthood
2023 Sep	50th European Muscle Conference University of Florence, Florence, Italy Oral and poster presentations: Sex-dependent progression of the *MYBPC1* E248K myopathy with tremor in response to aging
2023 May	The 27th Interdisciplinary Training Program in Muscle Biology Retreat University of Maryland School of Medicine, Baltimore, MD Oral presentation: Sex-dependent Progression of the *MYBPC1* E248K Myopathy with Tremor in Response to Aging
2023 March	45th Annual UMB Graduate Research Conference University of Maryland School of Medicine, Baltimore, MD Poster presentation: Sex-dependent Progression of the *MYBPC1* E248K Myopathy with Tremor in Response to Aging Awards: Geriatrics and Gerontology Education in Research Program Basic Science Research in Aging Student Award, GRC Outstanding Presentation Award

2023 January	Biochemistry and Molecular Biology Graduate Program in Life Science Retreat University of Maryland School of Medicine, Baltimore, MD Poster presentation: Sex-dependent Progression of the *MYBPC1* E248K Myopathy with Tremor in Response to Aging
2022 May	2022 Myofilament Meeting Monona Terrace Community and Convention Center, Madison, WI Poster presentation: *MYBPC1* E248K Myopathy Structural and Functional Development from Early through Late Adulthood
2022 March	2022 Annual UMB Graduate Research Conference University of Maryland School of Medicine, Baltimore, MD Poster presentation: Pathogenesis of *MYBPC1* E248K Myopathy During Aging

HONORS, AWARDS, & FELLOWSHIPS

2024 Apr	Graduate Research Conference Outstanding Presentation Award 46th Annual UMB Graduate Research Conference
2024 Mar	Global Travel Fellowship UMB Graduate Student Association
2023 Mar	Geriatrics and Gerontology Education in Research Program Basic Science Research in Aging Student Award 45th Annual UMB Graduate Research Conference
2023 Mar	Graduate Research Conference Outstanding Presentation Award 45th Annual UMB Graduate Research Conference
2020-2023	National Institute of Arthritis and Musculoskeletal and Skin Diseases (NIH-NIAMS), University of Maryland, Interdisciplinary Training Grant in Muscle Biology
2014-2015	Beta Beta Beta (Biological Sciences Honors Society) Loyola University Maryland
2011-2015	Joseph A. Selinger S.J. Scholarship Loyola University Maryland
2011-2015	Claver Scholarship Loyola University Maryland

TUTORING AND MENTORSHIP

2024 Spring	Co-mentor for rotation student Megan Perry; project title: "sMyBP-C localization and phosphorylation in *MYBPC1* E248K Myotrem mouse model"
2022 Spring	Mentor for rotation student Francisco Canale; project title: "sMyBP-C phosphorylation profile in E248K mouse model"
2019-2021	Tutor for Mechanisms in Biomedical Sciences Core Course
2019 Summer	Mentor for rotation student Aishwarya Iyer, project title: "Cloning, expression, and purification of mouse myosin S2"

ABSTRACT

Title of Dissertation: *MYBPC1* E248K Myotrem: an investigation into disease progression and pathogenic mechanisms

Jennifer Megan Canono Mariano, Doctor of Philosophy, 2024

Dissertation directed by: Aikaterini Kontrogianni-Konstantopoulos, PhD
Professor, Department of Biochemistry and Molecular Biology
University of Maryland School of Medicine

Myosin binding protein-C (MyBP-C) comprises a family of muscle accessory proteins that function in organizing and maintaining sarcomeric structure and regulating contractile function and actomyosin crossbridge cycling. Mutations in *MYBPC1*, the gene encoding the slow skeletal isoform (sMyBP-C), lead to a novel dominant form of myopathy termed Myotrem (OMIM: 318524) characterized by muscle weakness, congenital hypotonia, skeletal deformities, and characteristic tremor affecting the extremities and tongue. Due to the restricted expression of *MYBPC1* to skeletal muscle, as well as the absence of neuropathy in these patients, this tremor is believed to be a novel entity originating within the muscle itself. To further investigate Myotrem, our group has developed a murine model harboring a knock-in (KI) *MYBPC1* E248K mutation that faithfully recapitulates disease phenotype. Subsequent studies in KI muscle revealed that structural alterations of the sarcomere underlie the myopathy and are integral to pathogenesis. In human patients, Myotrem manifestations progress through childhood until adolescence, at which the phenotype stabilizes with no further deterioration. However, the clinical manifestation of Myotrem after mid-adulthood in response to the biological processes of aging is not known. In these studies, we used the murine KI model to perform *in vivo* contractile force measurements and quantitative structural analysis of immunofluorescence-stained muscle

to extensively characterize muscle structure and function in mid- and late-adulthood. We show that this stabilization period expires in late adulthood as KI mice show a decline in muscle structure and function in a sex- and muscle-specific manner where males and larger muscle muscles are more affected. Furthermore, although Myotrem tremorgenesis is considered to originate intrinsically in the muscle, the molecular mechanism is largely unknown. Notably, we found that permeabilized soleus fibers from KI mice exhibited unsolicited pulse activity with unprecedented regularity and persistence. Immunoblot and mechanical step-stretch experiments reveal that these pulsing KI fibers are slow-twitch in nature and display enhanced stretch activation properties. We posit that these pulsing fibers function as a myogenic pacemaker for tremor. Collectively, these studies provide essential information to inform patients afflicted with Myotrem of disease development and provide putative mechanisms for pathologic myogenic tremorgenesis.

MYBPC1 E248K Myotrem:
an investigation into disease progression and pathogenic mechanisms

by
Jennifer Megan Canono Mariano

Dissertation submitted to the faculty of the Graduate School of the
University of Maryland, Baltimore in partial fulfillment
of the requirements for the degree of
Doctor of Philosophy
2024

ACKNOWLEDGEMENTS

This work was made possible by the combined efforts and dedication of many individuals. I would like to thank my mentor, Dr. Aikaterini Kontrogianni-Konstantopoulos. I can't understate how grateful I am for the opportunity to train with you. Thank you for your guidance, patience, commitment to my growth, and for encouraging me to pursue things outside my comfort zone. I am honored to be part of the legacy of great scientists, and specifically women scientists, that had the privilege of receiving your mentorship. In addition, I am thankful to the members of my doctoral dissertation committee, Dr. Robert Bloch, Dr. Erick Hernandez-Ochoa, Dr. Bradford Percy, and Dr. Christopher Ward for your guidance. Your insight has been invaluable and your passion for science is inspiring. Thank you to my collaborators, including members of the Ward, Ochala, Joca, and McDonald labs, as well as the UMSOM core facilities such as the Confocal Microscopy Core and Musculoskeletal Physiology Service Center. Thank you to the staff and my fellow students of the Biochemistry and Molecular Biology department.

Furthermore, I would like to express gratitude to the members of the Kontrogianni Lab, both past and present. Thank you, lab fam, for your support every day and for sharing this journey with me. Most importantly, I thank my family and friends for their encouragement to pursue all my aspirations and for their constant support. Thank you to my parents, grandmother, and siblings being with me through all the ups and downs. Because of you all, I know I'll be able to take on any challenge. Finally, I'm thankful to God for the opportunity to explore this exciting topic, grow as a scientist, and share my findings with the community and beyond in hopes of improving human health and deepening our understanding of the world we live in. Proverbs 25:2

TABLE OF CONTENTS

LIST OF FIGURES

LIST OF ABBREVIATIONS

3T	3 Tesla
ANOVA	analysis of variance
ATP	adenosine triphosphate
BSA	bovine serum albumin
CD	circular dichroism
CK	creatine kinase
CMYP16	congenital myopathy-16
CNS	central nervous system
CT	computed tomography
DA-1	Distal arthrogryposis type 1
DEXA	dual energy x-ray absorptiometry
DRX	disordered relaxed
ECL	enhanced chemiluminescence
EDL	extensor digitorum longus
EEG	electroencephalography
EMG	electromyography
F	force
FFT	fast Fourier transform
F_{max}	maximal force
Fn-III	fibronectin-III
F_{res}	residual tension

GFP	green fluorescent protein
HCM	hypertrophic cardiomyopathy
HMM	Heavy meromyosin
IFM	indirect flight muscle
Ig	immunoglobulin
KD	knock-down
kDA	kilodalton
k_{df}	rate constant of delayed force development
KI	knock in
KO	knock-out
k_{rel}	rate constant of rapid force decay
k_{tr}	rate constat of tension redevelopment
LCCS-4	Lethal Congenital Contractual Syndrome-4
LDS	Lithium dodecyl sulfate
MD	molecular dynamics
MRC	Medical Research Council
MRI	magnetic resonance imaging
MyBP-C	myosin binding protein-C
NIH	National Institute of Health
P/A	proline/alanine
P_1 (mant -ATP)	amplitude of DRX population
P_1 (step-stretch)	maximal force
P_2 (mant -ATP)	amplitude of SRX population

P_2 (step-stretch)	minimal force
PBS	phosphate buffered saline
PKA	Protein kinase A
PKC	Protein kinase C
P_O	pre-stretch steady-state tension
P_{SS}	stretched-induced steady-state tension
P_{TO}	stretch-activated force *or* stretch-activation
ROI	region of interest
RyR1	ryanodine receptor 1
S2	subfragment 2
SDS	sodium dodecyl sulfate
SDS-PAGE	sodium dodecyl-sulfate polyacrylamide gel electrophoresis
SEM	standard error of the mean
Ser	serine
sMyBP-C	slow skeletal myosin binding protein-C
SPOC	spontaneous oscillatory contraction
SRX	staple
T_1	time constant of DRX population
T_2	time constant of SRX population
TA	tibialis anterior
Thr	threonine
WT	wild type
XRD	x-ray diffraction

CHAPTER 1

Myotrem: Clinical manifestations and investigations into molecular pathogenesis

1.1 Introduction

Myosin binding protein-C (MyBP-C) comprises a family of accessory sarcomeric proteins which function in sarcomere organization and maintenance and actomyosin crossbridge regulation (1, 2). The isoforms share a conserved core structure consisting of tandem immunoglobulin (Ig) and fibronectin-III (Fn-III) domains, as well as proline/alanine rich-region and a conserved M-motif at its NH_2-terminus end (2). Localized to the C-zone of the sarcomeric A-band, COOH-terminus constitutively binds the thick filament, while the NH2-terminus dynamically binds both actin and myosin to regulate crossbridge cycling (2, 3). The MyBP-C family is comprised of three isoforms: slow-skeletal and fast-skeletal, expressed in different combinations in both slow- and fast-twitch skeletal muscle, and cardiac, expressed in the heart, encoded by genes *MYBPC1*, *MYBPC2*, and *MYBPC3*, respectively (2). Much of what is known of MyBP-C has been discovered from studies on the cardiac isoform due to the high rate of *MYBPC3* mutations associated with congenital hypertrophic cardiomyopathies (HCM) (4). However, recently, there has been a growing interest in the slow skeletal isoform of MyBP-C due to its essential nature in skeletal muscle, complex modes of regulation, and its implication in disease (5).

sMyBP-C is an essential protein in muscle development and function. Expressed ubiquitously in both slow- and fast-twitch muscles, sMyBP-C uniquely plays a primarily structural role in tissues (6). *MYBPC1* knock-down (KD) in adult mouse FBD, and

constitutive and induced *MYBPC1* knock-out (KO) in mouse pups and adult mice, respectively, lead to major structural alterations including thick filament damage, major effects in the transcription of sarcomeric structural genes, and consequently deficits in contractile function and force production (6, 7). Parallel to the cardiac isoform, sMyBP-C also undergoes post-translational modification with residues Ser-59, Ser-62, Ser-83, Thr-84, and Ser-204 as targets for PKA and/or PKC phosphorylation (8). However, unique to the slow skeletal isoform, *MYBPC1* undergoes extensive alterative splicing, giving rise to at least 14 known splice variants in humans (gene ID 4606) and 18 splice variants in the mouse (gene ID 109272) which are co-expressed in the same fiber, with ratios varying between muscle tissue types (1, 9). Splice variant expression and phosphorylation status create unique muscle- and age-profiles which are implicated in disease, such as distal arthrogryposis type-1 (DA-1) and muscular dystrophy (9-11).

Recently, *MYBPC1* and its role as a pathogenic gene has garnered much attention (5). Causal mutations have been identified that lead to forms of congenital arthrogryposis including DA-1 and lethal congenital contractual syndrome 1 (LCCS) (5, 12, 13). Recently, our group in collaboration with others has identified a group of mutations in *MYBPC1* that co-segregate with a new form of myopathy characterized by tremor (14, 15). Restriction of *MYBPC1* expression to the skeletal muscle paired with absence of neuropathy in these patients lead us to believe that this is a new tremor entity originating intrinsically in the muscle (14, 16, 17). Since its first description in 2019, a total of five dominant pathogenic polymorphisms have been identified: Y247H (14), E248K (14, 18), L259P (15), L263R (15, 18-20), and L219P (21). Interestingly, all mutations exist in the M-motif, a region responsible for dynamic binding of both actin (22) and the S2 sub-fragment of heavy

meromyosin (HMM) (23). This form of myopathy with myogenic tremor has been recently recognized as an independent disease entity, termed "Myotrem" (OMIM: 618524), or Congenital Myopathy 16 (CYMP16). Herein, we provide a comprehensive update on the clinical manifestations of Myotrem and a summary of the studies investigating disease pathogenesis.

1.2 Myotrem Clinical Manifestations

1.2.1 Myogenic Tremor

The most common and characteristic manifestation defining Myotrem is tremor of myogenic origin (14, 15, 18-21). The tremor is most commonly present in the extremities, most noticeable in the arms and hands, and to a lesser extent in the legs and feet (14, 15, 18). A facial and lingual tremor is also reported in the tongue and lips (14, 15, 18). In a few pediatric cases, tremor was also reported to be present in the trunk and the whole body (15, 21). It's described as a predominantly postural tremor and accentuated upon intention or exertion (14, 15, 18, 20, 21). The tremor also exists at rest in some patients, primarily in the tongue (15, 18). Tremor is described as irregular with generally low amplitude and high frequency (14, 15, 18, 21). Absence of tremor was only described in one patient harboring the L219P polymorphism (21). This polymorphism interestingly is the only Myotrem mutation present in the intrinsically disordered region of the M-motif and has variable penetrance even in individuals of the same family, exhibiting various Myotrem and other non-related phenotypes to differing degrees (21).

Electromyography (EMG) or ultrasonography studies were performed on some of Myotrem individuals and a myopathic pattern and/or tremor was confirmed in five of seven

patients (14, 15, 19-21). Spontaneous activity was not reported for any of the tested individuals (14, 20). Of interest is a particular EMG study outfitted with accelerometers followed by quantitative tremor analysis performed by Stavusis *et al.* on a family harboring the Y247H polymorphism (14). In three patients, accelerometry readings on outstretched hands did not change frequency with loading of the hands, suggesting that there is a central nervous component of the tremor. In addition, there was a lack of intracorporal tremor synchronicity observed in a few patients. One patient showed differing frequencies in hand tremor between their left and right arms, described in clinical observations and confirmed with EMG studies. Dual-channel EMG studies in another patient revealed a lack of temporal synchronicity between both legs, suggesting to the authors the presence of multiple tremor pacemakers within the body.

1.2.2 Generalized Myopathy

In addition to tremor, patients show mild generalized myopathy manifesting as hypotonia and muscle weakness. Hypotonia was described in all reported Myotrem polymorphisms (14, 15, 18-21). For a few family members harboring the L263R polymorphism, congenital hypotonia was considered severe in newborns that a diagnosis of spinal muscular atrophy was considered before exclusion following negative genetic testing (15). Hypotonia greatly improved during early development and through adolescence but persists to some degree in adulthood (15). Strength was most affected in proximal muscles of the upper arms and pelvic area (14, 15, 18, 20, 21), but also axial (14), facial (18), and distal (21) muscle groups in other cases. Myotrem muscle weakness was considered mild with Medical Research Council (MRC) muscle strength grading ranging

between 4- and 5- (20, 21). Other skeletal-muscle related symptoms such as myalgia, cramping, atrophy, and calf pseudohypertrophy have been reported in individuals with the Y247H and L219P mutations (14, 21).

Effects on motor function are evident with variable expressivity. During development, most patients show a delay in gross motor milestone acquisition with head bobbing (14, 15, 18), feeding difficulties (15, 19), and delayed independent ambulation (1, 14, 15, 18, 21). Hypersomnolence and poor fine motor skills have been described in two different patients harboring the L259P and L219P polymorphisms, respectively (15, 21). These symptoms often resolved over time, with tremor and general myopathic symptoms persisting without further deterioration after adolescence (14, 15, 19). While some individuals report no significant interference in daily activities (14, 15, 18, 20, 21), poor muscular performance persists in others, manifesting as easy fatigability, poor stamina, and exercise intolerance. For example, a 27-year-old patient with a L263R polymorphism required the use of a wheelchair for long walks (15). A 58-year-old patient with the L219P mutation reports difficulty performing sit-to-stand movements and lifting objects overhead (21). Muscle weakness, sometimes in the presence of contractures, led to atypical gait in some patients, such as stepping gait (14), waddling gait (15, 18, 19), and toe walking (21).

One study using muscle computed tomography (CT) imaging, did not reveal any remarkable findings in a patient with the L263R polymorphism (18). However, a separate study performed by Leduc-Pessah *et al.*, used muscle-specific 3 Tesla (3T) magnetic resonance imaging (MRI) technology to obtain high-quality whole-body images of individuals harboring the L219P polymorphism (21). These studies revealed a pattern of fatty infiltration, fat saturation, and fat stranding in some muscles including the tongue,

gluteus muscles, paravertebral muscles, and deltoid and biceps. Interestingly, muscles were affected differently within the same patient, where paravertebral muscle, gluteus medius and gluteus minimus muscles exhibited atrophy, while gastrocnemius and soleus muscles exhibited hypertrophy. 3T MRI did not reveal evidence of muscle edema.

Patient biopsy samples were limited but underwent histopathological analysis and fiber typing. Evaluation of Y247H deltoid muscle showed type I dominance and type I fiber smallness in cross-sectional area (14). Myogenic damage as well as mitochondrial proliferation was found in the deltoid muscles of a patient with the L263R mutation, as well as decreased sMyBP-C expression levels (18).

1.2.3 Additional manifestations

Patients afflicted with Myotrem often develop skeletal deformities, thought to be secondary to muscular dysfunction, such as scoliotic phenotypes (14, 18), including lordoscoliosis (19) and curvature of the thoracolumbar regions (21), as well as general spinal rigidity and thoracic asymmetry (14, 19). Two patients, harboring the Y247H or L263R polymorphisms also presented with mild bilateral scapular winging (14, 19). Contractures have been described in three Myotrem mutations, affecting the elbows and ankles (14, 21), but are more commonly absent in patients.

Myotrem also often leads to mild dysmorphia of facial muscles, leading to phenotypes including long thin face (15), depressed nasal bridge (18), and prominent nasolabial folds (14). Ptosis and a down-slanted palpebral fissure have been described in three cases (14, 21). Open mouth (18), pouting lips (14), micrognathia and microstomia (14), high-arched palate (14, 19), and cleft lip (18) have also been reported.

Respiratory effects have been described, such as stridor in a 5-year-old patient with the L259P polymorphism (15). Stridor has also been reported in a 23-month-old patient, which has improved, but who also has developed tachypnea (18). Reports of frequent respiratory infections and paradoxical breathing have been described in Myotrem patients harboring the E248K mutation (14). Sleep gas levels measured in a patient with the L263R polymorphism showed normal O_2 levels with slightly elevated CO_2 levels (19).

Myotrem's effect on the reproductive system is not yet fully understood. One patient with the L219P was also diagnosed with polycystic ovarian syndrome and had a history of spontaneous abortions (21). Furthermore, a patient with the E248K mutation was required to deliver two children via cesarean section due to the position of her pelvis (18). Both children also inherited the E248K polymorphism, with intrauterine growth restrictions reported during the fetal development of the younger child (18).

Notably, Myotrem patients show no evidence of neuropathy. Cognitive function (14, 15, 19, 20), coordination (20), and sensation (20, 21) has been largely described as normal with deep tendon reflexes intact (15, 18, 19, 21). Nerve conduction studies (14, 15, 18, 19, 21), brain MRI (15, 19, 20), and electroencephalography (EEG) (15, 20) have shown no remarkable findings. Although some exceptions are reported, Myotrem is not believed to affect the nervous system (17). Likewise, cardiac (14, 19, 21), ocular (14, 15, 21), and auditory (14) functions are usually unaffected. Metabolic tests are typically normal (15, 19, 24) with no remarkable changes in serum creatine kinase (CK) levels (19, 21). Hyperthyroidism was reported in two patients, with accompanying hyperprolactinemia as well as early macular degeneration in one patient harboring the L219P mutation (21). The lack of a neural and cardiac phenotype is consistent with the fact that the expression of

MYBPC1 is limited to skeletal muscle and supports the theory of a tremor of myogenic origin.

1.3 Investigation into Myotrem molecular pathogenesis

1.3.2 *In vivo* murine model

Using CRISPR/Cas9 technology, our group developed a murine model harboring a knock-in (KI) point mutation *Mybpc1* E249K, corresponding to the human *MYBPC1* E248K mutation. This is the only published Myotrem mouse model to date. Studies were performed by Hauserman *et al.* and published in 2020 (24). To avoid confusion, this model will be referred to as the E248K KI model. Homozygous inheritance of the mutation was neonatally lethal, with pups showing signs of respiratory distress and dying a few hours after birth. Experiments performed in young and adult mice were therefore performed with heterozygous mice, congruent with human patients who are all heterozygous. The KI model was found to faithfully recapitulate Myotrem phenotype and disease development observed in human patients. A battery of behavioral assays on young mice up to 8 weeks of age, including open field, ataxia box, and inverted hang, revealed defects consistent with generalized myopathy. Plethysmography revealed deficits in peak inspiratory flow, paralleling respiratory infections observed in humans and X-ray imaging of 6-month-old adult mice revealed the development of kyphosis, mirroring the development of skeletal deformities and scoliosis.

KI mice were smaller in total body weight, isolated muscle weight and muscle cross-sectional area. Electrophysiological and biomechanical studies in EDL further

confirmed contractile deficits in force generation and kinetics. *Ex vivo* studies in intact EDL revealed decreased specific force generation, normalized to muscle mass, as well as slower rates of contraction and relaxation, that emerged at higher stimulation frequencies. A similar pattern was also observed in diaphragm strips. *In vitro* studies of permeabilized EDL fibers also exhibited decreased passive tension, decreased absolute and normalized maximum calcium-activated tension in pCa 4.5 solutions, and decreased power in loaded shortening experiments.

Interestingly, there were no significant differences in fiber type distribution, and slack-restretch experiments revealed no significant difference in the rate of tension redevelopment of crossbridges (K_{tr}) between WT and KI fibers. In addition, although tension-pCa experiments in permeabilized EDL fibers revealed a shift in calcium sensitivity and calcium signaling experiments in intact EDL showed alterations in KI muscle, that were inconsistent with the contractile deficits observed. However, the most striking difference observed was in sarcomeric structure. Immunofluorescence studies revealed many out-of-register sarcomeres due to split and laterally misaligned fibers in both EDL and soleus KI tissue. On the ultrastructural level, KI fibers exhibited less compact Z-, A-, I-, and M-bands, Z-disk streaming, enlarged mitochondria, and internal membrane fragmentation. Quantification of sagittal sections revealed a decrease in the average cross-sectional area of myosin filaments and a decrease in average interfilament distance. These findings are consistent with the primary role of sMyBP-C as a structural protein and suggest that sarcomeric disorganization is integral to the mechanism(s) underlying Myotrem.

1.3.3 Binding studies

Interestingly, all known Myotrem polymorphisms are located within the M-motif, a portion responsible for transient interactions between the thick and thin filament (2, 22, 23). Overlay assays were used to assess recombinant GST-tagged constructs of WT or Myotrem Y247H or E248K mutations binding to purified HMM and actin immobilized on nitrocellulose (14). Both Myotrem mutants showed enhanced binding to HMM and trended to show increased binding to actin. HMM-binding was enhanced ~2- and ~3.5-fold compared to WT for the Y247H and E248K mutations, respectively. These *in vitro* studies were corroborated by computation modeling which predicted that the Y247H and E248K substitutions would strengthen and stabilize electrostatic interactions with HMM (14).

Similar GST-tagged recombinant constructs of the NH_2-terminal portion of sMyBP-C through the M-motif were generated with and without the presence of L259P or L263R mutations (15). Here, binding to HMM was assessed using surface plasmon resonance (SPR) to determine binding affinity (K_D). Interestingly, the constructs demonstrated opposing effects, where introduction of the L259P mutation did not greatly alter HMM binding compared to WT, while the L263R mutation decreased binding ~5.5 fold. These results were corroborated by blot overlay (15). Actin-binding was subsequently assessed using blot overlay and revealed no significant changes when compared to WT (15).

It is interesting to note that all four residues exhibit differential, and in some cases antithetical, binding to myosin and actin, yet all result in the similar Myotrem phenotype. Although altered actin and/or myosin binding is thought to underlie the pathogenic mechanism(s) of Myotrem, further studies are required to understand the mutation-specific

effects on macromolecular binding and the differential effects leading to a similar pathogenic effect on organ and whole-body levels.

1.3.4 Structural studies and *in silico* molecular modeling

Molecular modeling was used to predict the effect of Myotrem mutations on M-motif structure. Although the structure of the slow-skeletal isoform is not yet known, the model of the cardiac isoform (80% identify) was used as a template, which identifies a disorder disordered region followed by a ~35-residue tri-helix bundle (25). Circular dichroism (CD) studies with recombinant M-motif suggests a similar helicity in in the slow-skeletal isoform as well.

Studies performed by Stavusis *et al.,* report structural studies focusing on the Y247H and E248K mutations (14). These residues are present in an area with local positive charge. Myotrem mutations in these locations would effectively increase this local positive charge by either introducing the protonable imidazole ring of the histidine residue or by replacing a negatively charged glutamic acid residue with a positively charged lysine.

Similar MD and CD studies regarding the L259P and L263R mutations and reported by Shashi *et al.* (15). Residues L259 and L263 are predicted to be located within the third helix of the tri-helix bundle (15). A proline substitution in residue 259 is likely to disrupt the helicity the bundle via steric hindrance, as predicted by molecular dynamics (MD) stimulation. This is supported by reduced helicity in CD studies and increased cleavage in trypsin digestion assays (15). Residue L263 is modeled to be present within the hydrophobic core and a substitution by positively charged arginine is predicted to disrupt the hydrophobic core and decrease the stability of the tri-helix bundle. This is

supported by CD studies showing L263R mutant unfolding at lower temperatures when compared to WT.

Studies investigating the L219P substitution were performed by Leduc-Pessah *et al.,* using AlphaFold and other web-based tools such as Group-based Prediction System, Predictor of Natural Disordered Regions, and DynaMut (21). This residue is present in the predicted intrinsically disordered region if the protein, upstream of the trihelix bundle. These tools predicted that introduction of the mutation would increase disorder and molecular flexibility in the local area but did not predict any changes regarding interactions or large structural deformities.

1.4 Discussion

The growing standardization of the use of genomic sequencing technologies to assist with clinical diagnosis has allowed for the identification of novel genes associated with rare diseases (26) and likely accelerated the recognition of Myotrem as its own independent entity. However, there is still no known effective therapy for these patients, warranting the need to understand the molecular effects of these mutations and the mechanisms of disease pathogenesis. Moreover, current understanding of disease progression is based on clinical evidence as reported by afflicted individuals, presenting with a severe phenotype during childhood, which resolves to mild myopathy after adolescence and remaining stable through mid-adulthood. However, given the limited age range of known patients, we do not know if this stabilization period persists into late adulthood. Given what we know about the changes in sMyBP-C splice variant expression

and phosphorylation profiles with aging (10, 11), the progression of Myotrem in late adulthood potentially may result in a change pathogenic phenotype with age.

The most distinguishing feature of this myopathy is tremor which is believed to be of myogenic origin due to the restricted expression of *MYBPC1* to skeletal tissue and the absence of neuropathy in these patients (16). As most known tremors are though to originate due to deficits in the nervous system, this concept of a tremor originating in the muscle itself is novel and not yet fully understood. (14). Most clinical cases of tremor, such as essential and neuropathic tremor, are neuropathic in origin, or tremor secondary to neurological disease such as Parkinson's. As such, the current pharmacological treatments for tremor are believed to target nervous system (27). In contrast, Myotrem tremor results from pathogenic mutations in sarcomeric *MYBPC1* with the pacemaker residing in the muscle itself (17), which may explain why these current pharmacological options are not effective for Myotrem patients. In addition to *MYBPC1*, pathogenic polymorphisms in other sarcomeric genes of both the thick and thin filaments such as *MYH7*, *MYH2*, *MYL2, TNNT1*, *NEB*, and *TMP3* have also been linked to forms of myopathy with tremor (16). However, the molecular mechanism(s) for myogenic tremorgenesis are still unknown. The use of *in vivo* models such as the E248K murine model will be helpful in investigating such mechanisms as well as exploring potential effective therapeutics.

Despite manifestation as the similar Myotrem pathology in patients, different causal *MYBPC1* mutations show differential molecular effects on binding and structure. For example, while the E248K mutation shows enhanced binding to HMM (14), the L263R mutation shows an antithetical decreased binding (15). In addition, although the structure of the human slow-skeletal M-motif is not yet solved, predictions based on the cardiac M-

motif place four of the five mutations are in the ordered helical region and the L219R mutation in the disordered region (14, 15, 21). This may underlie the diversity in expressivity of the family harboring the L219R polymorphism between other individuals afflicted with Myotrem as well as between family members with the same genotype. Moreover, a patient diagnosed with DA-1 is described as exhibiting Myotrem-related manifestations such as hypotonia and facial dysmorphia resulting from compound heterozygote variant in the C7 and C8 domains of sMyBP-C, further highlighting the complexity of sMyBP-C pathogenesis (28). Additional studies are required to understand the mutation-specific effects on sMyBP-C structure and binding on the atomic and molecular levels and how they contribute to Myotrem clinical manifestations.

Herein, we use the *MYBPC1* E248K murine model to investigate aspects of Myotrem disease progression into late adulthood and pathogenic mechanisms of myogenic tremor. The *MYBPC1* E248K model faithfully recapitulates Myotrem disease progression and phenotype and can serve as a powerful tool for studying *in vivo* effects of Myotrem-causing mutation. We characterize the Myotrem phenotype in terms of sarcomeric structure and consequential contractile function in mid- and late adulthood to better understand disease progression in response to aging. These studies provide insight to the patients and their care providers regarding how Myotrem is predicted to progress in human patients as well. In addition, we use the E248K model to investigate the mechanism of a myogenic tremor and uncover unsolicited contractile activity in myofibers, independent of neural stimulation. Together, these studies address two important and previously unknown aspects of Myotrem with the hope of broadening our understanding of this myopathy to help provide an effective therapy to afflicted individuals.

CHAPTER 2

Sex-dependent progression of the *MYBPC1* E248K Myotrem myopathy in response to aging

This chapter is a research article submitted in May 2024 to the Journal of Clinical Insight. It was returned with favorable reviews was invited for resubmission. I served as first author and contributed to conceptualization, data curation, formal analysis, investigation, methodology, validation, visualization, writing the original draft, and reviewing and editing. This study also constitutes work from the labs of Dr. Chris Ward, PhD, who contributed to conceptualization and contractility studies, Dr. Humberto Joca, PhD, who helped develop and perform quantitative structural analysis, and Dr. Julien Ochala, PhD, who performed the single nucleotide turnover assays.

2.1 Introduction

Myosin binding protein-C (MyBP-C) comprises a family of sarcomeric accessory proteins expressed in striated muscles that have structural and regulatory roles by contributing to thick filament assembly and maintenance, and modulating actomyosin crossbridge formation and kinetics (1, 2, 9, 29-31). MyBP-C proteins are mainly composed of tandem immunoglobulin and fibronectin-III-like domains, but also contain a proline-alanine (P/A) rich region, and a highly conserved M-motif (32). Localized to the C-zone of the sarcomeric A-band, the COOH-terminus of MyBP-C is constitutively bound to the thick filament, while the NH_2-terminus interacts dynamically with both myosin and actin filaments to regulate actomyosin crossbridge formation. The MyBP-C family consists of

three distinct isoforms: slow skeletal, fast skeletal, and cardiac. *MYBPC1*, the gene encoding the slow skeletal isoform, is heavily spliced to give rise to at least 17 known splice variants in humans (1). These variants are co-expressed in both slow and fast skeletal myofibers in different combinations, ratios and amounts and may have structural and/or regulatory roles (9).

MYBPC1 has garnered increasing interest due to its recognition as an essential myopathic gene (5). Our group has recently identified novel pathogenic variants in *MYBPC1* whose monoallelic presence leads to a new form of myopathy characterized by tremor. The absence of neuropathy in the afflicted patients and the restricted expression of sMyBP-C to skeletal muscles implicate a myogenic origin of the tremor (16), coining the term Myotrem myopathy (NIH concept ID: C5231401) or congenital myopathy-16 (CMYP16) (14, 15). In addition to tremor in the upper and lower extremities, Myotrem carriers exhibit hypotonia, muscle weakness, lagged gross motor milestone acquisition, and delayed independent walking (achieved at approximately two-years of age). Affected individuals also develop skeletal deformities presenting as spinal rigidity, scoliosis, and/or thoracic asymmetry, contractures in the elbows, and frequent respiratory infections (14).

The Myotrem phenotype manifests in infancy and progresses through childhood, entering a stabilization phase in adolescence with no further deterioration during early adulthood (14). As the majority of the diagnosed Myotrem patients range in age between early childhood to early adulthood, it remains unclear if this plateau phase persists in mid and late adulthood and whether Myotrem patients exhibit increased vulnerability to the inevitable consequences of aging.

Our lab has developed and characterized a murine Myotrem model harboring the *MYBPC1* E248K pathogenic variant (24). Homozygous inheritance of the E248K variant is neonatally lethal, likely due to respiratory failure leading to cyanosis (24). However, heterozygous animals survive and develop Myotrem myopathy that faithfully recapitulates the onset, manifestation, and progression of the disease through young adulthood, seen in human carriers (14, 24). Accordingly, heterozygous knock in (KI) E248K neonates exhibit a high frequency tremor both at rest and during locomotion, that subsides in young adulthood and is evident only upon intention (24). Moreover, young adult KI mice exhibit generalized myopathy, impaired neuromuscular performance, diminished force production, and structural alterations manifesting as out-of-register sarcomeres, diffuse A-, I-, and M-bands, enlarged mitochondria, and Z-disk streaming (24). Consistent with the key structural role of sMyBP-C (7, 29), it has been postulated that the observed sarcomeric deficits are likely the primary contributing factor of the E248K Myotrem myopathy (24).

Given that the E248K model is a reputable proxy of Myotrem development and manifestation, we set forth to investigate muscle structure and function in mid (12-months) and late (24-months) adulthood, aiming to learn if and how Myotrem progresses following stabilization during adolescence. Excitingly, our studies show a sex-dimorphic progression of E248K Myotrem pathology with aging, underscored by distinct biochemical, structural, and functional alterations. Our study therefore uncovers essential information with translational implications about the effects of biological sex and age in Myotrem presentation, severity, and underlying pathologies.

2.2 Results

2.2.1 Phenotypic and behavioral evaluation of the MYBPC1 E248K murine model in mid- and late adulthood

To characterize the age-dependent progression of the *MYBPC1*-associated Myotrem myopathy, we utilized the established E248K murine model that we previously generated (24). No difference in survival was observed across 4-weeks to 24-months of age between WT and heterozygous KI animals for both males **(Fig. 2.1A)** and females **(Fig. 2.1B)**. Using a battery of phenotypic and behavioral assays, we set forth to study the manifestation and progression of the E248K Myotrem myopathy by profiling muscle structure/function at 12- and 24-months, corresponding to mid (40-45 human years) and late (70-75 human years) adulthood, respectively (33). Males and females were analyzed separately, and KI animals were compared to age- and sex-matched WT littermates.

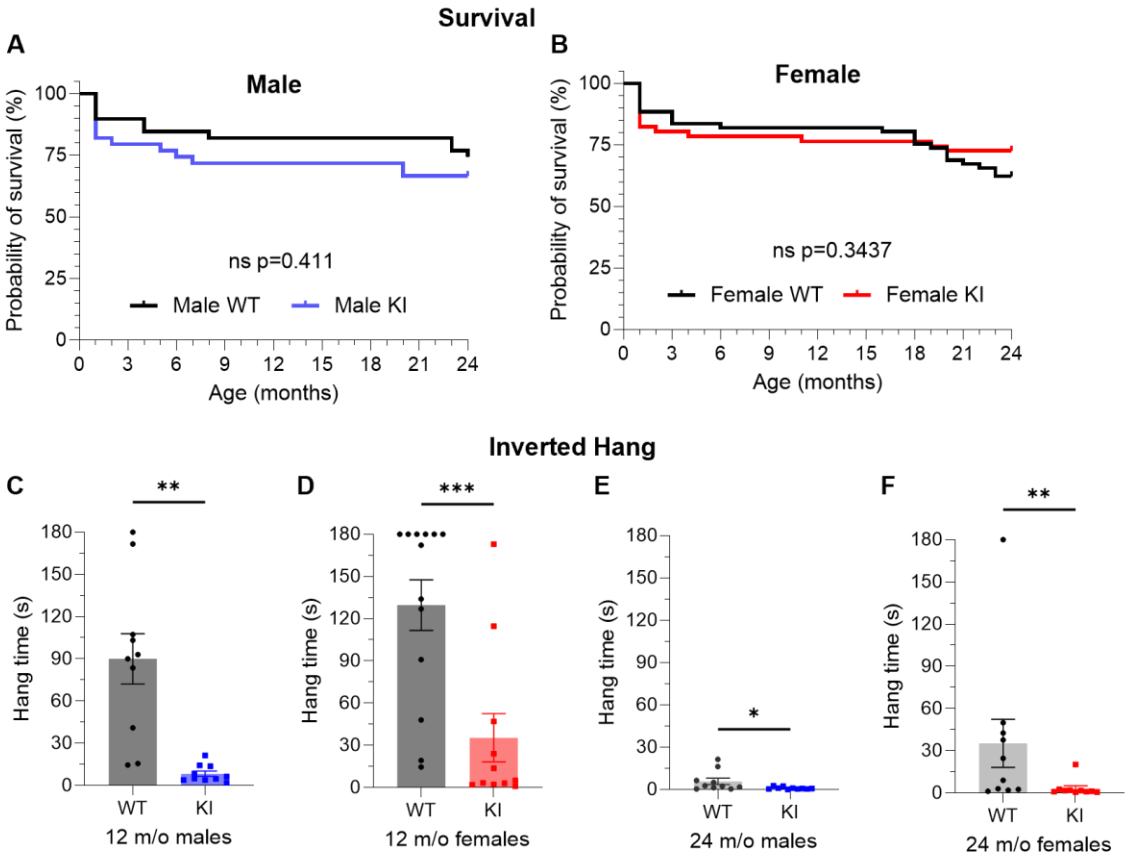

Figure 2. 1 Survival and neuromuscular performance evaluation of E248K KI Myotrem mice in mid- and late adulthood.
(A) Kaplan-Maier curves show no difference in survival rates between WT and KI animals, independently of biological sex, between 4-weeks to 24-months of age; log-rank test, males: p=0.603, *n*=39 per genotype; females: p=0.344, *n*=59 WT, *n*=51 KI. **(B)** Overall coordination, endurance, and neuromuscular performance were assessed by inverted hang assay. KI animals consistently performed worse than their age-and sex-matched WT littermates; 12-month-old males: *n*=10 per genotype, 24-month-old males: *n*=10 per genotype, 12-month-old females: *n*=13 WT, *n*=11 KI; 24-month-old females: *n*=10 per genotype. Data is presented as mean ± SEM and statistical significance was determined by Welch's *t*-test **(C)** or Mann-Whitney *t*-test **(D-F)**; **p*<0.05, ***p*<0.01, and ****p*<0.001.

Gross neuromuscular performance assessed by an inverted hang test identified significant deficits in both male and female KI mice at 12- and 24-months compared to their sex- and age-matched WT littermates **(Fig. 2.1 C-F),** consistent with generalized neuromuscular impairment. Musculoskeletal quality and body composition were also evaluated using dual energy x-ray absorptiometry (DEXA). At 12-months, KI males tend

to be more kyphotic **(Fig. 2.2 A-B)**, and exhibit significantly reduced body and fat mass **(Fig. 2.2 C-D)**, yet higher lean mass **(Fig. 2.1 D),** compared to their WT counterparts. As male E248K mice age to 24-months, these features are largely preserved **(Fig. 2.1 E-H)**. Conversely, female KI mice are significantly more kyphotic at 12-months **(Fig. 2.1 I-J**), but display similar body **(Fig. 2.1 K)**, lean, and fat **(Fig. 2.1 L)** mass relatively to their WT littermates. At 24-months, female KI mice retain their kyphotic presentation **(Fig. 2.1 M-N)**, but are significantly smaller **(Fig. 2.1 O)** and leaner with lower fat mass **(Fig. 2.1 P)**, compared to sex- and age-matched WT. Thus, although the two sexes share some deficiencies (e.g., neuromuscular impairment), they also develop distinct manifestations (e.g., skeletal abnormalities and body composition) as a function of aging.

Figure 2. 2 Phenotypic evaluation of aging E248K Myotrem mice using DEXA measurements. DEXA measurements were performed in 12-month-old males **(A-D)**, 24-month-old males **(E-H)**, 12-month-old females **(I-L)**, and 24-month-old females **(M-O)**. **(A, E, I, & M)**: Representative DEXA scans show body and skeletal morphology; scale bar: 2 cm. **(B, F, J, & N)**: The extent of spinal curvature is quantified by determining the kyphotic index by calculating the ratio of the distance between the C7 and L6 vertebrae and the length of a perpendicular line reaching the extreme dorsal curvature of the spine, indicated by the dotted yellow line in the WT mouse in **(A)**. Kyphotic index trends to be higher in 12- and 24-month-old KI males **(B & F)** and is significantly elevated in 12- and 24-month-old KI females **(J & N)**, when compared to age- and sex-matched WT mice; n=8 males per age/per genotype, n=5 12-month-old females per genotype, n=6 24-month-old WT females, n=5 24-month-old KI females. **(C, G, K, & O)**: Total mass measurements indicated that KI animals have either significantly (i.e., 12-month-old males and 24-month-old females) or trending (24-month-old males and 12-month-old females) smaller mass compared to their age- and sex-matched WT littermates. **(D, H, L, & P)**: KI male animals are consistently leaner than their age-matched WT counterparts at both 12-months **(D)** and 24-months **(H)** of age. While WT and KI female animals exhibit comparable levels of lean mass at 12-months **(L)**, by 24-months, they are markedly leaner than their age- and sex-matched WT littermates **(P)**; n=11 12-month-old WT males, n=8 12-month-old KI males, n=9 24-month-old WT males, n=8 24-month-old KI males, n=21 12-month-old WT females, n=8 12-month-old KI females, n=8 24-month-old WT females, n=7 24-month-old KI females. Data is presented as mean ± SEM and statistical significance was determined by 2-tailed Student's t-test **(B-D, J-K, N & P)**, with Welch's correction when appropriate **(G & O)**, or Mann-Whitney t-test **(F, H, & L)**; ns: not significant, *$p<0.05$ and **$p<0.01$.

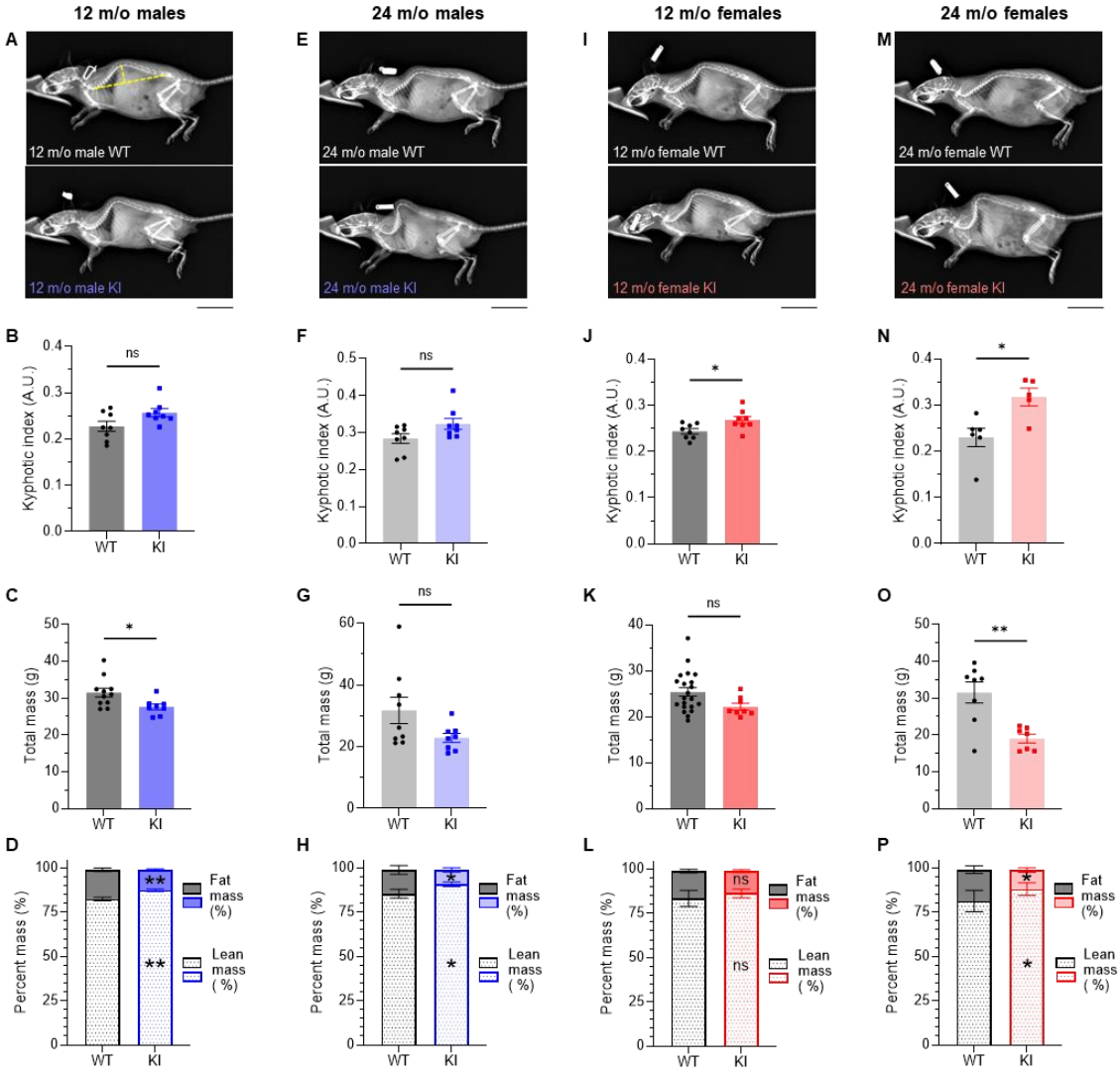
12 m/o males
24 m/o males
12 m/o females
24 m/o females
A
E
I
M
12 m/o male WT
12 m/o male KI
24 m/o male WT
24 m/o male KI
12 m/o female WT
12 m/o female KI
24 m/o female WT
24 m/o female KI
B
F
J
N
Kyphotic index (A.U.)
ns
*
WT
KI
C
G
K
O
Total mass (g)
**
D
H
L
P
Percent mass (%)
Fat mass (%)
Lean mass (%)

2.2.2 Evaluation of sarcomeric structure, myosin relaxation state, and contractile function in 12-month-old E248K Myotrem mice

Given the essential role of sMyBP-C in myofibrillar assembly and maintenance (7, 29), we evaluated sarcomeric organization and sMyBP-C localization in tibialis anterior (TA) muscle. Images of WT and KI TA muscle sections were immunostained for the Z-disk marker α-actinin and sMyBP-C **(Fig. 2.3 A, B, C & D, E, F),** subjected to quantitative analysis, and scored for levels of sarcomeric breakage, continuity, and order **(Fig. 2.3 B'-B" & E'-E"),** and sMyBP-C localization **(Fig. 2.3 C'-C" & F"-F")**, respectively. The breakage, continuity, and order scores were collectively used to reflect either prototypic sarcomeric organization **(Fig. 2.4 A)** or distinct patterns of sarcomeric abnormalities, including lateral misalignment, sarcomeric continuum, disordered organization, and chaotic organization **(Fig. 2.4 B-E)**.

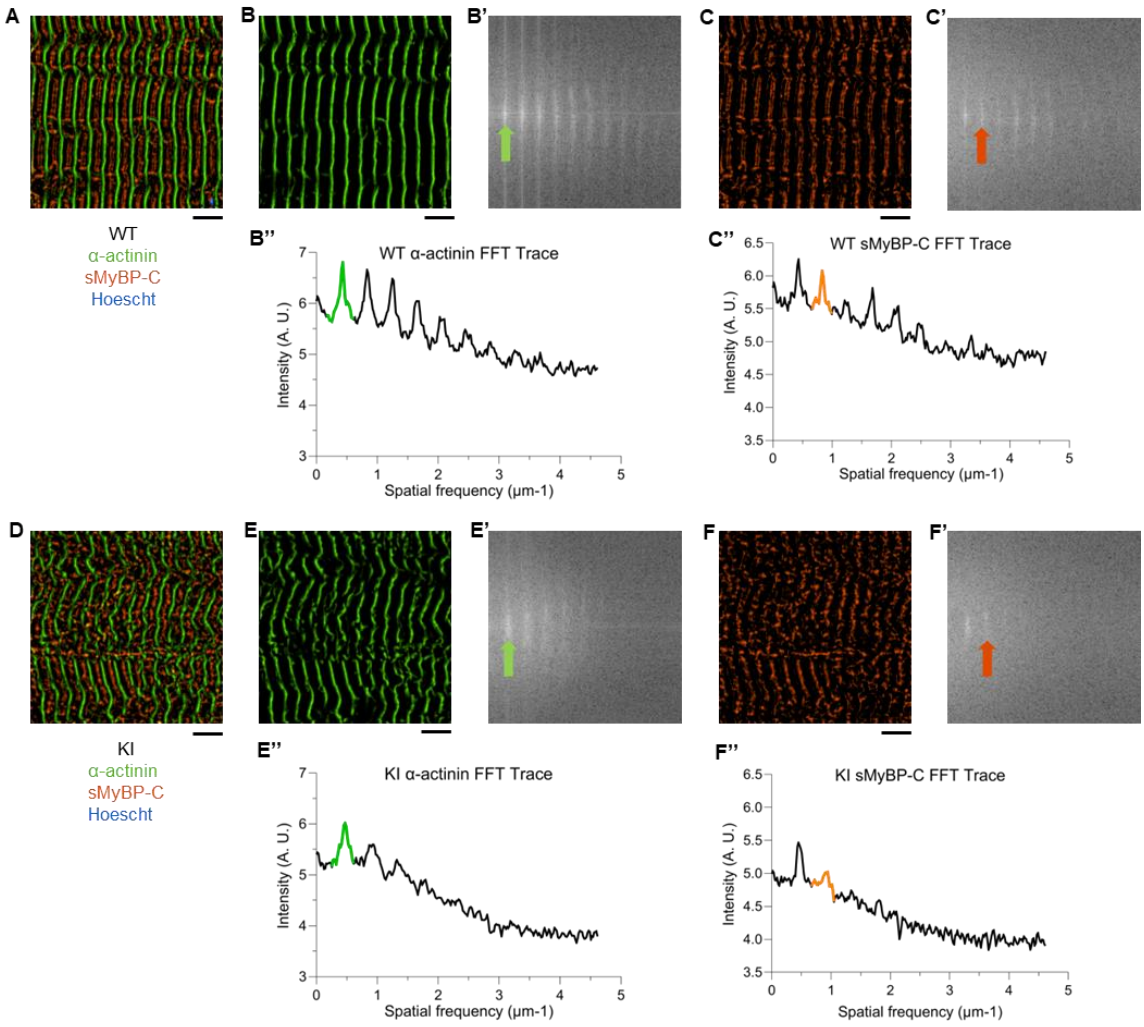

Figure 2. 3 Quantification of sarcomeric organization and sMyBP-C localization via FFT analysis.

(A, B, C & D, E, F) Representative images of tissue sections from 24-month-old male WT **(A, B, C)** and KI **(D, E, F)** TA muscles co-stained for α-actinin **(B & E)** and sMyBP-C **(C & F)** were used to determine sarcomeric order and sMyBP-C localization scores, respectively. To calculate the order score, α-actinin-stained images **(B & E)** underwent FFT analysis followed by generation of the respective power spectra **(B' & E')**. The signal intensity along the longitudinal axis was plotted **(B" & E")** allowing for visualization of distinct peaks. The first peak, indicated by the green arrow on the power spectra **(B' & E')** and marked in green on the FFT traces **(B" & E")** corresponds to overall sarcomeric order, while the value of the amplitude of the first peak is reported as the order score. Similarly, to determine the sMyBP-C localization score, sMyBP-C images **(C & F)** underwent FFT analysis **(C' & F')**, and the intensity profiles were plotted **(C" & F")**. The second peak, indicated by the red arrow on the power spectra **(C' & F')**, and denoted in red on the FFT traces **(C" & F")** corresponds to sMyBP-C localization to the C-zone, while the value of the amplitude of the second peak is reported as the sMyBP-C localization score.

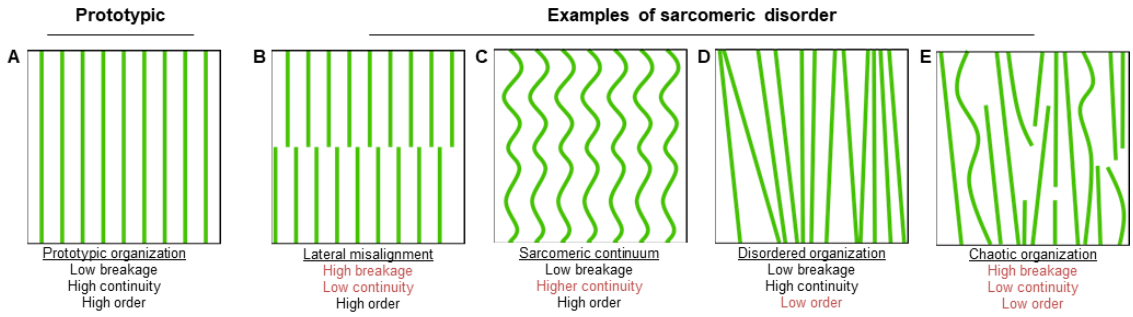

Figure 2. 4 Examples of sarcomeric organization metrics.
Cartoon representation of sarcomeric organization patterns using α-actinin immunostaining. **(A)** Prototypic sarcomeric organization is characterized by low breakage and high continuity and order scores. **(B-E)** Types of disordered sarcomeric organization and metric changes relatively to the prototypic organization, described as **(B)** lateral misalignment, resulting in increased breakage, decreased continuity, and unchanged order scores; **(C)** sarcomeric continuum, resulting in unchanged breakage and order scores, but increased continuity score; **(D)** disordered organization, resulting in unchanged breakage and continuity scores, but reduced order score; and **(E)** chaotic organization, resulting in higher breakage and lower continuity and order scores. These classifications of sarcomeric (dis)organization were used to deduce the breakage, continuity and order scores described in Figs 2, 4, 6, & 8, following FFT analysis of α-actinin immunostaining as described in Supplemental Fig. 2.

Although areas of apparent disorganization were observed in KI TA male muscles at 12-months of age (**Fig. 2.5 A**), quantification of overall sarcomeric structure revealed comparable levels of myofibrillar breakage **(Fig. 2.5 B)**, continuity **(Fig. 2.5 C)**, and order **(Fig. 2.5 D)** between WT and KI, indicating an overall preservation of prototypic sarcomeric organization. Relatedly, sMyBP-C was properly localized to the C-zone of A-bands in both WT and KI male muscles **(Fig. 2.5 A & E-F)**, while its levels remained unaltered throughout aging **(Fig. 2.6 A-C)**.

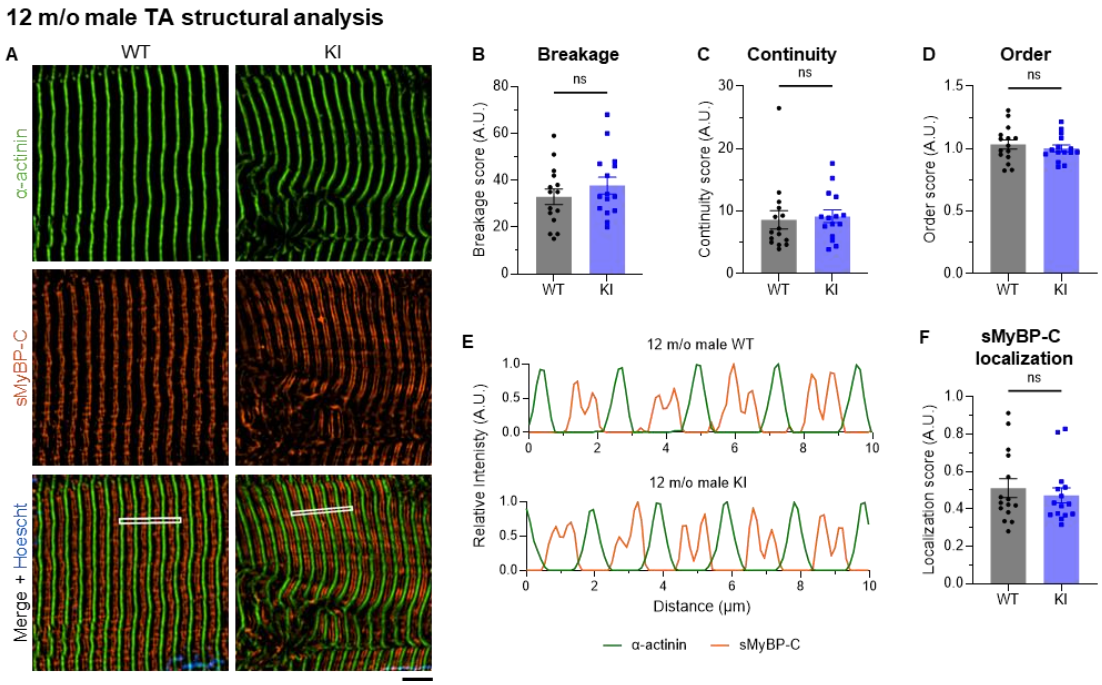

Figure 2. 5 Quantitative evaluation of sarcomeric structure in 12-month-old male TA tissue. **(A)** Representative images of TA muscle sections labeled for α-actinin and sMyBP-C; scale bar: 5 μm. Quantification of overall myofibrillar structure performed on α-actinin-stained images revealed comparable breakage **(B)**, continuity **(C)** and order **(D)** scores between WT and KI TA male muscles at 12-months. **(E)** Linear profiles of α-actinin and sMyBP-C relative intensities confirmed their alternating distribution, corresponding to Z-disk and C-zone localization, respectively; the ROIs used for analysis are denoted with a white rectangle in the merged images. **(F)** sMyBP-C exhibited similar localization scores in WT and KI TA male muscles at 12-months, as determined via FFT analysis. *n*=3 male mice per genotype and *n'*=5 images per muscle. Data is presented as mean ± SEM and statistical significance was determined with 2-tailed Student's *t*-test **(B & D)** or Mann-Whitney *t*-test **(C & F)**; ns: not significant.

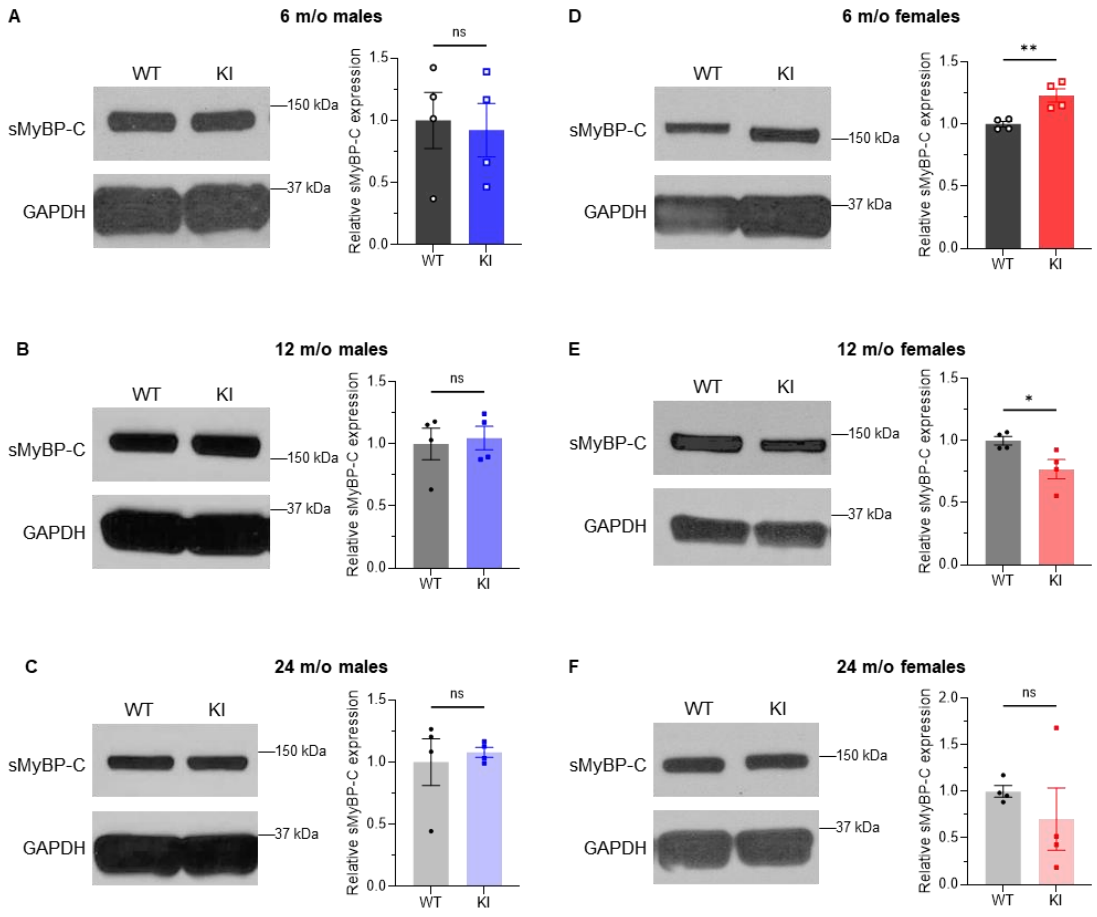

Figure 2. 6 Immunoblot analysis of sMyBP-C expression levels in E248K TA muscles through aging.
Representative immunoblots probed for sMyBP-C levels using lysates prepared from male **(A-C)** and female **(D-F)** TA muscles at 6- **(A & D)**, 12- **(B & E)**, and 24-months of age **(C & F)**. Quantification is relative to sex- and age-matched WT. **(A-C)** Male KI TA muscles express the same levels of sMyBP-C compared to WT at 6-, 12-, and 24-months of age. On the contrary, female KI TA muscles show significantly increased sMyBP-C expression at 6-months **(D)**, which reverts to marked reduction at 12-months **(E)** and remains as a strong decreasing trend at 24-months **(F)**; n=4 mice per sex/per age/per genotype. Data is represented as mean ± SEM and statistical significance was determined by 2-tailed Student's t-test **(A-B & D-E)**, with Welch's correction when appropriate **(C & F)**; ns: not significant, *p<0.05 and **p<0.01.

As MyBP-C has been implicated in the regulation of the relaxation state of myosin (34-36), we proceeded to determine biochemically the ratio of myosin heads in disordered-relaxed (DRX; defined by faster ATPase activity and higher force-generating potential) *versus* super-relaxed (SRX; defined by slower ATPase activity and lower force-generating potential) state, using Mant-ATP chase single nucleotide turnover assays. Similar ratios and

lifetimes of myosin heads in DRX (P_1, T_1) *versus* SRX (P_2, T_2) states were measured between WT and KI TA myofibers from 12-month-old male mice **(Supplemental Fig. 5A-E)**.

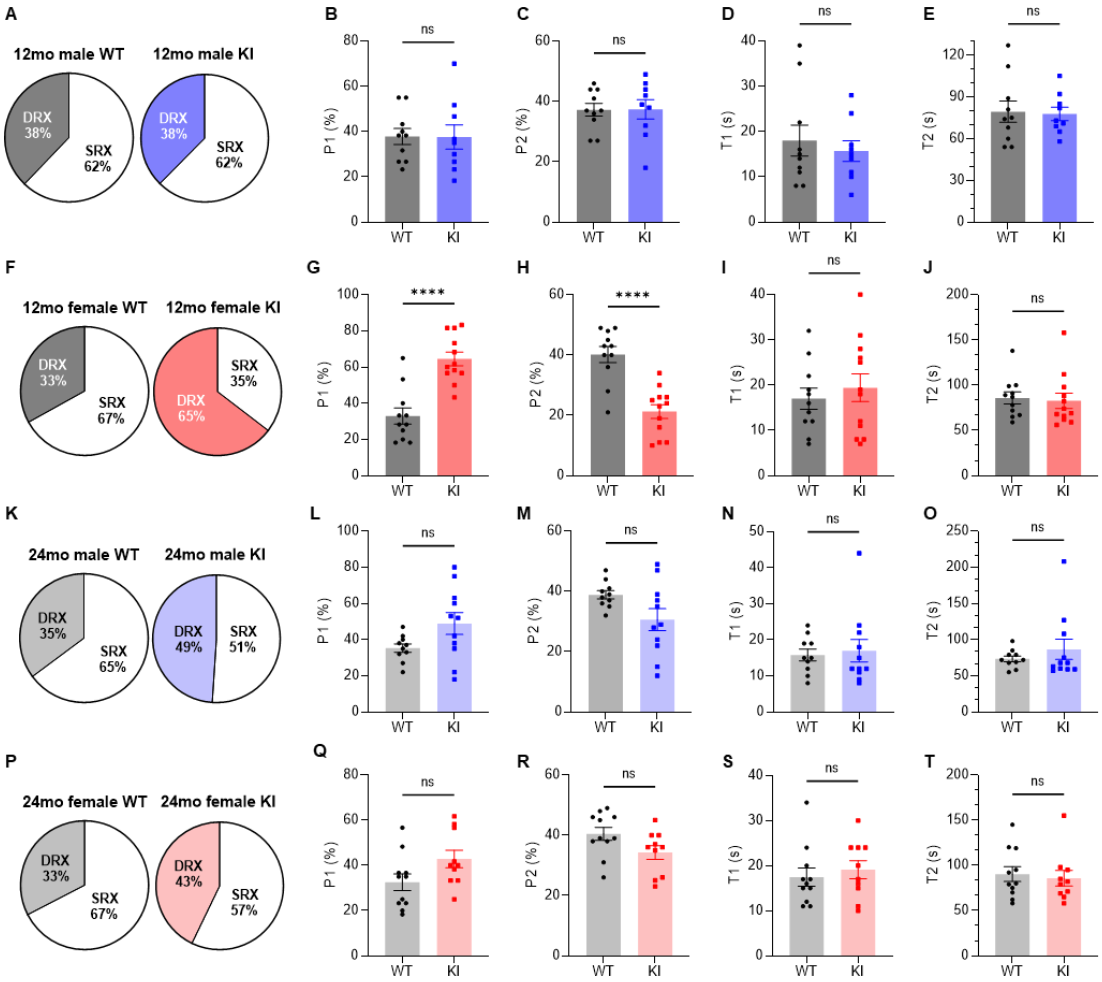

Figure 2. 7 Determination of the DRX:SRX myosin ratio in E248K TA myofibers using single nucleotide turnover Mant-ATP chase assay.
The average proportion of myosin heads in the DRX versus SRX state was calculated in both male and female WT and KI TA myofibers at 12- **(A & F)** and 24- **(K & P)** months of age. Individual values of the DRX population (P_1; **B, G, L, & Q)** and lifetime (T_1; **D, I, N, & S)** and the SRX population (P_2; **C, H, M, & R)** and lifetime (T_2; **E, J, O, & T)** were also obtained. WT and KI TA male myofibers exhibit similar DRX:SRX proportions and lifetimes at both 12- **(A-E)** and 24- **(K-O)** months of age. Conversely, KI TA female myofibers contain a significantly higher DRX:SRX ratio compared to WT at 12-months **(F-H)**, which is not sustained though at 24-months **(P-R)**. The lifetimes of the DRX and SRX states remain unchanged at both ages **(I-J & S-T)**; n=2 animals per sex/per age/per genotype and n'=9-12 fibers per muscle. Data is presented as mean ± SEM and statistical significance was determined by 2-tailed Student's t-test **(B-C, E, G-I, & Q-R)**, with Welch's correction when appropriate **(L-M)**, or Mann-Whitney t-test **(D, J, N-O, & S-T)**; ns: not significant, and ****p<0.0001.

The contractile performance of TA muscle from 12-month-old WT and KI male animals was subsequently assessed using an *in vivo* system in which the hindlimb was immobilized, the peroneal nerve was percutaneously stimulated between 1-150 Hz to evoke isometric contractions, and the resulting force was measured to produce force-frequency plots **(Fig. 2.8)**. We focused on measurements at tetanic (150 Hz) stimulation, which is biologically relevant to voluntary motor activity (37-39). Despite a decrease in isolated muscle mass **(Fig. 2.8 A)** exhibited by KI male muscles at 12-months, no significant contractile differences between WT and KI TA male muscles were observed at 12-months with regards to absolute tetanic force **(Fig. 2.8 B-C)**, specific tetanic force (calculated by dividing the absolute tetanic force with the muscle mass) **(Fig. 2.8 D)**, and contractility kinetics **(Fig. 2.8 E-F)**, a consistent trend indicative of functional decline was witnessed across all measurements.

Figure 2. 8 *In vivo* nerve-evoked isometric force measurements of 12-month-old male TA muscle.
Contractility was assessed using *in vivo* nerve-evoked isometric contractions. WT and KI mice were anesthetized, the hindlimb was immobilized, and the common peroneal nerve was percutaneously stimulated by brief (500 msec) trains of pulses delivered at 1 to 150 Hz. **(A)** Isolated TA muscle mass was smaller KI males when compared to WT males at 12-months. **(B)** Representative force traces of TA dorsiflexion of WT and KI 12-month-old mice resulting from 150 Hz stimulation. **(C, left)** Force *versus* stimulation frequency curve. A trending decline was observed in absolute tetanic force (150 Hz; **C, right**), specific tetanic force calculated by dividing the absolute tetanic force with the muscle mass **(D),** and the rates of contraction **(E)** and relaxation **(F)** in male KI TA muscles at 12-months compared to sex- and age-matched WT; n=10 male mice per genotype. Data is presented as mean ± SEM and statistical significance was determined by Mann-Whitney t-test **(A)**, 2-way ANOVA followed by Šidák's test for multiple comparisons **(C & D)**, or 2-tailed Student's t-test **(E & F)**; ns: not significant and *$p<0.05$.

12 m/o male TA contractile function

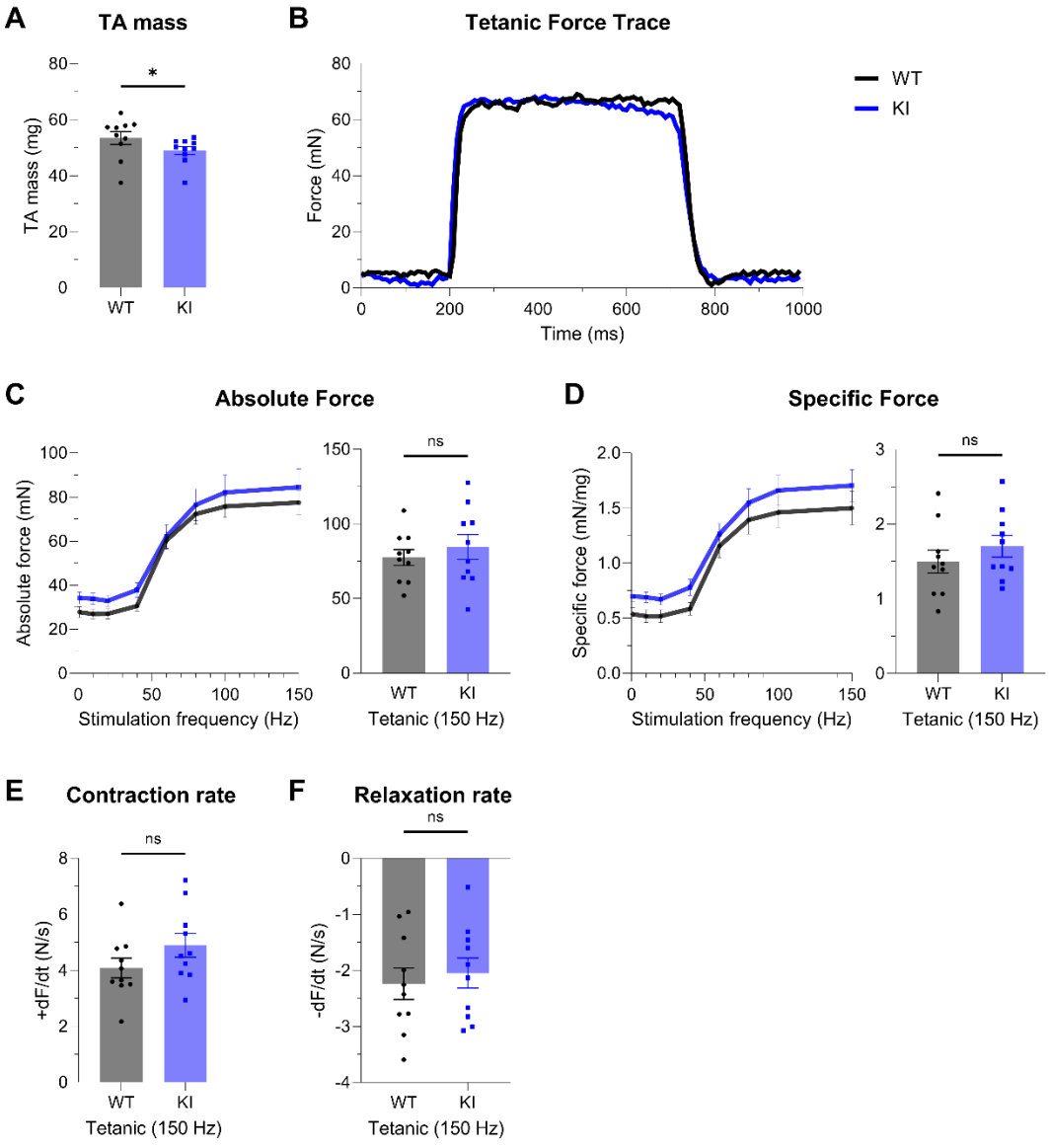

The structural organization, myosin relaxation state, and contractile performance of female muscles was interrogated, too, at 12-months. Accordingly, WT and KI female TA muscles immunostanined for α-actinin **(Fig. 2.9 A)** displayed similar levels of myofibrillar breakage **(Fig. 2.9 B)**, continuity **(Fig. 2.9 C)**, and order **(Fig. 2.9 D)**, consistent with a prototypic sarcomeric organization **(Fig. 2.4 A).** Likewise, sMyBP-C was properly targeted to the C-zone in muscles from both genotypes **(Fig. 2.9 A & E-F)**. Contrary to males however, a significant upregulation in the levels of sMyBP-C was detected in female KI TA muscles at 6-months **(Fig. 2.6 D)**, which reverted to notable reduction at 12-months, relatively to WT **(Fig. 2.6 E).** Interestingly, while no apparent structural abnormalities **(Fig. 2.9)** accompanied the decreased levels of sMyBP-C in KI female TA muscles at 12-months, a significant increase of myosin heads in the energy-consuming DRX state **(Fig. 2.7 F-G)** and a reciprocal decrease in the energy-saving SRX state **(Fig. 2.7 F & H)** was observed, when compared to sex- and age-matched WT, while the T_1 and T_2 lifetimes remained unaltered **(Fig. 2.7 I-J)**. This gain in the DRX state of myosin heads was likely reflected in *in vivo* evaluation of the contractile performance of KI TA female muscle, which exhibited comparable mass **(Fig. 2.10 A)**, absolute tetanic force **(Fig. 2.10 B-C)**, specific force **(Fig. 2.10 D)**, and contractility kinetics **(Fig. 2.10 E-F)** with WT tissue, and lacked the trending functional decline observed in male KI TA muscle at the same age **(Fig. 2.8)**.

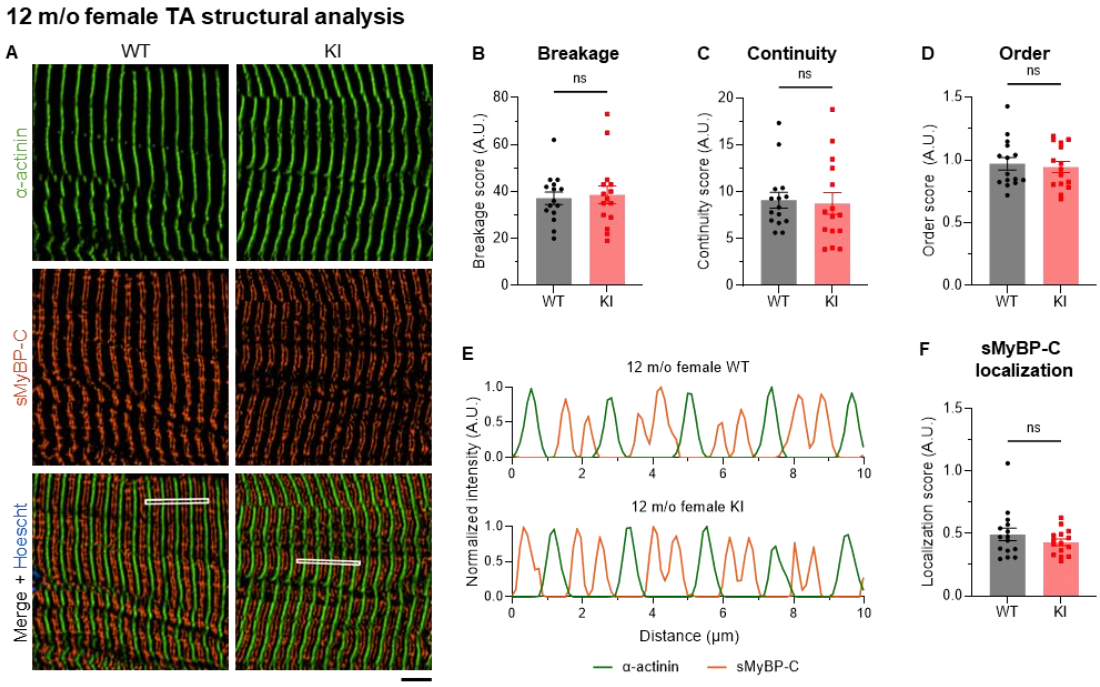

Figure 2. 9 Quantitative evaluation of sarcomeric structure in 12-month-old female TA tissue. **(A)** Representative images of TA muscle sections immunostained for α-actinin and sMyBP-C; scale bar: 5 μm. At 12-months, KI female TA muscle exhibits similar levels of breakage **(B)**, continuity **(C)**, and order **(D)** to age- and sex-matched WT tissue. **(E)** Relative intensity profiles of α-actinin and sMyBP-C confirmed their alternating distribution, corresponding to Z-disk and C-zone distribution, respectively; the ROIs used for analysis are indicated with a white rectangle in the merged images. **(F)** sMyBP-C exhibited comparable localization scores between WT and KI TA female muscles at 12-months, as calculated via FFT analysis. *n*=3 female mice per genotype and *n'*=5 images per muscle. Data is presented as mean ± SEM and statistical significance was determined by 2-tailed Student's *t*-test **(B & D)** or Mann-Whitney *t*-test **(C & F)**; ns: not significant.

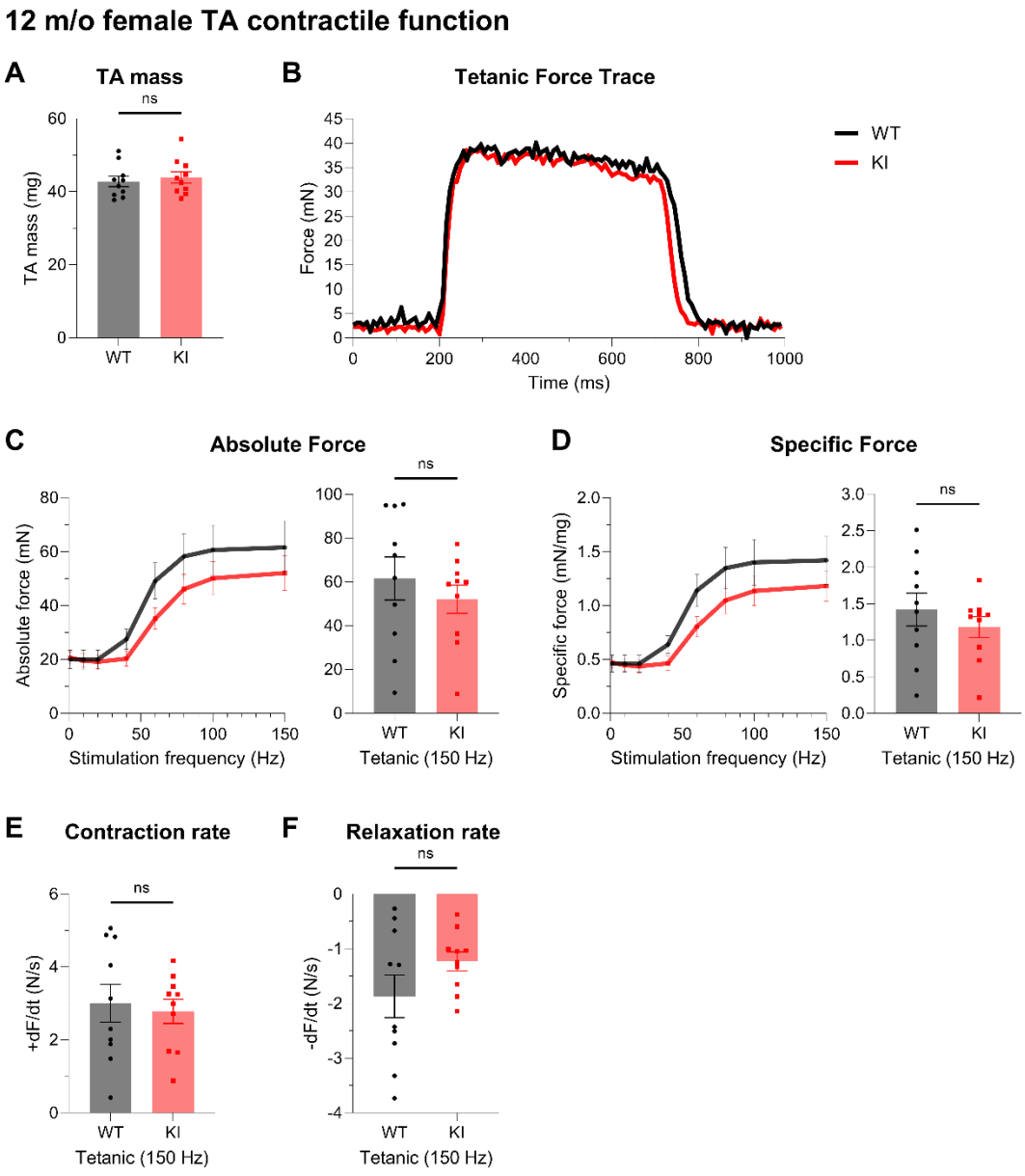

Figure 2. 10 *In vivo* nerve-evoked isometric force measurements of 12-month-old female TA muscle.
Contractility was assessed using *in vivo* nerve-evoked isometric contractions. The common peroneal nerve was percutaneously stimulated by brief (500 msec) trains of pulses delivered at 1 to 150 Hz. KI female TA muscles exhibited comparable mass **(A)** and developed similar absolute tetanic force **(B-C),** specific tetanic force **(D)**, and contraction **(E)** and relaxation **(F)** kinetics to WT; *n*=10 female mice per genotype. Data is presented as mean ± SEM and statistical significance was determined by 2-tailed Student's *t*-test **(A & E)**, 2-way ANOVA followed by Šidák's test for multiple comparisons **(C & D)**, or Welch's *t*-test **(F)**; ns: not significant.

Together, these findings demonstrate the presence of a prolonged stabilization phase of the E248K Myotrem myopathy that extends into mid adulthood. Although the

disease manifestation is largely akin between the two sexes at this stage, there are key distinctions pertinent to an emerging contractile decline in KI males, and a likely adaptive increase in the DRX myosin state accompanied by a concomitant decrease of sMyBP-C expression in KI females.

2.2.3 Characterization of sarcomeric structure, myosin relaxation state, and contractile function in 24-month-old E248K Myotrem mice

To investigate whether the plateau phase persists in late adulthood, we proceeded to evaluate the E248K Myotrem model at 24-months of age. Interestingly, examination of the structural organization of KI TA male muscles using α-actinin immunostaining uncovered severe structural deficits **(Fig. 2.11 A)**. These were quantitatively reflected as higher breakage score **(Fig. 2.11 B)**, and lower continuity **(Fig. 2.11 C)** and order **(Fig. 2.11 D)** scores compared to sex- and age-matched WT tissue, indicative of a pattern of chaotic organization **(Fig. 2.4 E).** Consistently, sMyBP-C assumed a disordered distribution in KI TA male muscle at 24-months **(Fig. 2.11 A)**, failing to assemble in the typical C-zone doublets seen in WT muscle **(Fig. 2.11 A & E).** This was further substantiated by the markedly lower localization score of sMyBP-C in KI tissue compared to sex- and aged-matched WT **(Fig. 2.11 F).** Similar to 12-months, sMyBP-C expression was indistinguishable between WT and KI TA male muscles at 24-months **(Fig. 2.6 C)**. Moreover, although no statistical differences were detected in the DRX:SRX ratio of myosin heads **(Fig. 2.7 K-M)** or their respective T_1:T_2 lifetimes **(Fig. 2.7 N-O)**, an upward trend of myosin heads in the DRX state was observed in KI muscles, likely as a late adaptive response.

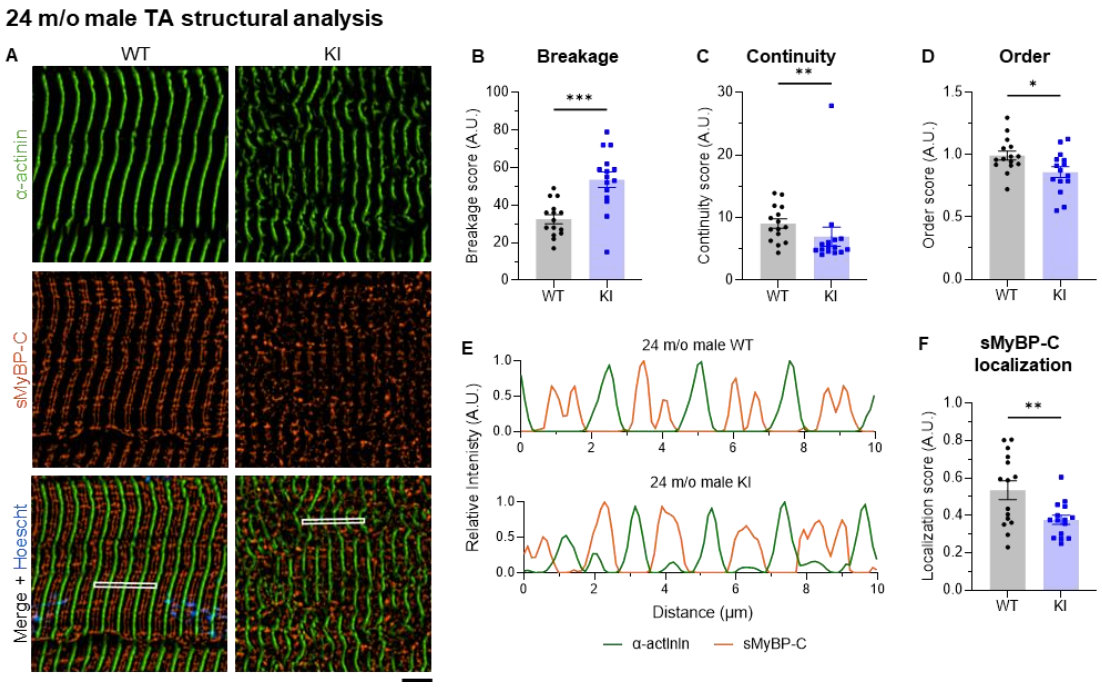

Figure 2. 11 Quantitative evaluation of sarcomeric structure in 24-month-old male TA tissue. **(A)** Representative images of TA muscle sections labeled for α-actinin and sMyBP-C; scale bar: 5 μm. Contrary to 12-months, at 24-months KI male TA muscles displayed significantly increased breakage **(B)** and markedly decreased continuity **(C)** and order **(D)** scores compared to sex- and age-matched WT tissue. Consistently, sMyBP-C failed to occupy the typical C-zone doublets, as shown in linear plots of the relative intensity profiles of α-actinin and sMyBP-C **(E;** ROI used for analysis is outlined by a white rectangle in the merged images**)**, and the significantly reduced sMyBP-C localization score of KI TA muscles compared to WT **(F)**; n=3 male mice per genotype and n'=5 images per muscle. Data is presented as mean ± SEM and statistical significance was determined by 2-tailed Student's t-test **(B & F)** or Mann-Whitney t-test **(C)**; *p<0.05, **p<0.01, and ***p<0.001.

Importantly the structural abnormalities documented in KI TA male muscles at 24-months were accompanied by contractile deficits *in vivo*. Although KI TA muscle exhibited similar mass to sex- and age-matched WT **(Fig. 2.12 A)**, it produced significantly reduced absolute **(Fig. 2.12 B-C)** and specific **(Fig. 2.12 D)** tetanic force reflecting diminished intrinsic force generative capacity, and suppressed contractility kinetics as evidenced by the dampened contraction **(Fig. 2.12 E)** and prolonged relaxation **(Fig. 2.12 F)** rates.

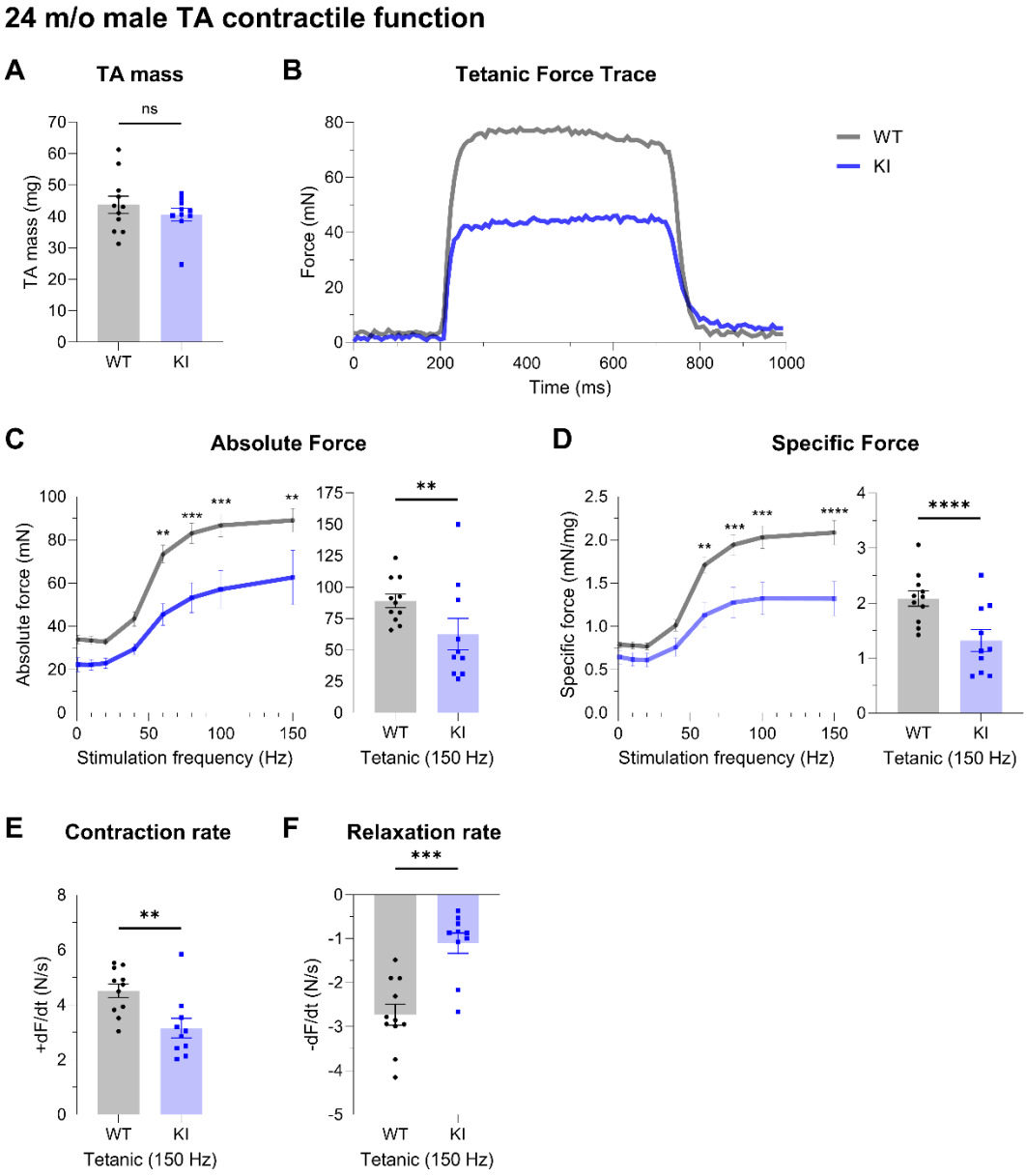

Figure 2. 12 *In vivo* nerve-evoked isometric force measurements of 24-month-old male TA muscle.

Contractility was assessed using *in vivo* nerve-evoked isometric contractions. The common peroneal nerve was percutaneously stimulated by brief (500 msec) trains of pulses delivered at 1 to 150 Hz. **(A)** The muscle mass of WT and KI TA male muscles was similar at 24-months. However, KI TA muscle developed significantly reduced absolute tetanic force **(B-C)**, specific force **(D),** and contraction **(E)** and relaxation **(F)** rates compared to age- and sex-matched WT tissue; n=11 WT and n=10 male mice per genotype. Data is presented as mean ± SEM and statistical significance was determined by Mann-Whitney t-test **(A & F)**, 2-way ANOVA followed by Šidák's test for multiple comparisons **(C & D)**, or 2-tailed Student's t-test **(E)**; ns: not significant, *p<0.05, **p<0.01, and ***p<0.001.

In stark contrast to male KI TA muscle, female KI TA muscle displayed no gross sarcomeric abnormalities at 24-months, as evidenced by immunostaining for α-actinin **(Fig. 2.13 A)** and quantified by comparable breakage **(Fig. 2.13 B)** and order **(Fig. 2.13 D)** scores with sex- and age-matched WT. Interestingly though, the continuity score was significantly elevated in KI tissue relatively to WT **(Fig. 2.13 C)**, suggestive of a wavelike pattern of structural (mal)adaptation, characterized by enhanced sarcomeric continuum **(Fig. 2.3 C)**. Moreover, sMyBP-C occupied the sarcomeric C-zone in female TA muscles of both genotypes **(Fig. 2.13 A & E)**, as indicated by their similar localization scores **(Fig. 2.13 F)**. Notably, the significant reduction in sMyBP-C levels observed in KI TA female muscles at 12-months **(Fig. 2.6 E)** is not sustained at 24-months, as it turns into a decreasing trend **(Fig. 2.6 F)**. Likewise, the marked upregulation of the DRX:SRX ratio of myosin heads found in KI TA female muscles at 12-months **(Fig. 2.7F-H)** is not replicated at 24-months but becomes an increasing trend **(Fig. 2.7 P-R)** with no changes in T_1 and T_2 lifetimes **(Fig. 2.7 S-T)**.

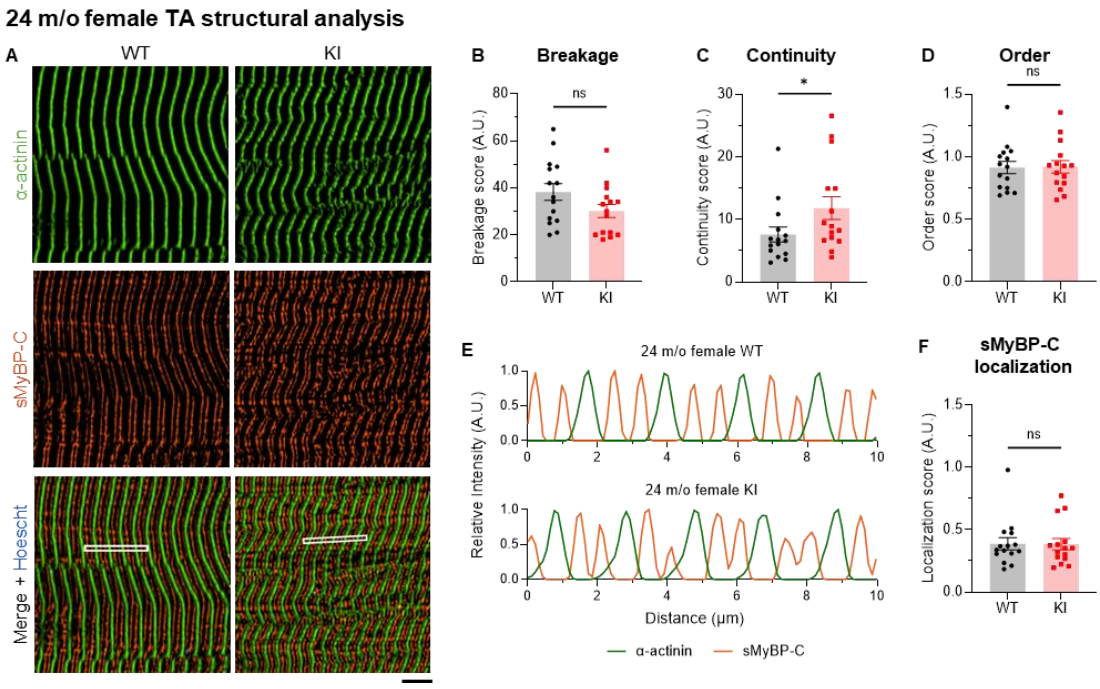

Figure 2. 13 Quantitative evaluation of sarcomeric structure in 24-month-old female TA tissue.
Representative images of TA tissue sections were immunolabeled for α-actinin and sMyBP-C; scale bar: 5 μm. Relatively to WT female TA muscles, KI muscles exhibited comparable breakage **(B)**, increased continuity **(C)**, and similar order **(D)** scores. Moreover, sMyBP-C assumed its typical doublet distribution at sarcomeric C-zones in both WT and KI TA muscles, as shown in linear plots of the relative intensity profiles of α-actinin and sMyBP-C **(E;** ROI used for analysis is marked with a white rectangle in the merged images**)**, and similar sMyBP-C localization scores **(F)**; n=3 female mice per genotype and n'=5 images per mouse. Data is presented as mean ± SEM and statistical significance was determined by 2-tailed Student's t-test **(B & D)** or Mann-Whitney t-test **(C & F)**; ns: not significant and *p<0.05.

Consistent with the presence of a sustained stabilization phase in aging female E248K Myotrem mice, WT and KI TA muscles exhibit similar mass **(Fig. 2.14A)** and develop comparable levels of absolute **(Fig. 2.14 B-C**) and specific **(Fig. 2.14 D)** tetanic force, characterized by equivalent rates of contraction **(Fig. 2.14 E)** and relaxation **(Fig. 2.14 F)**.

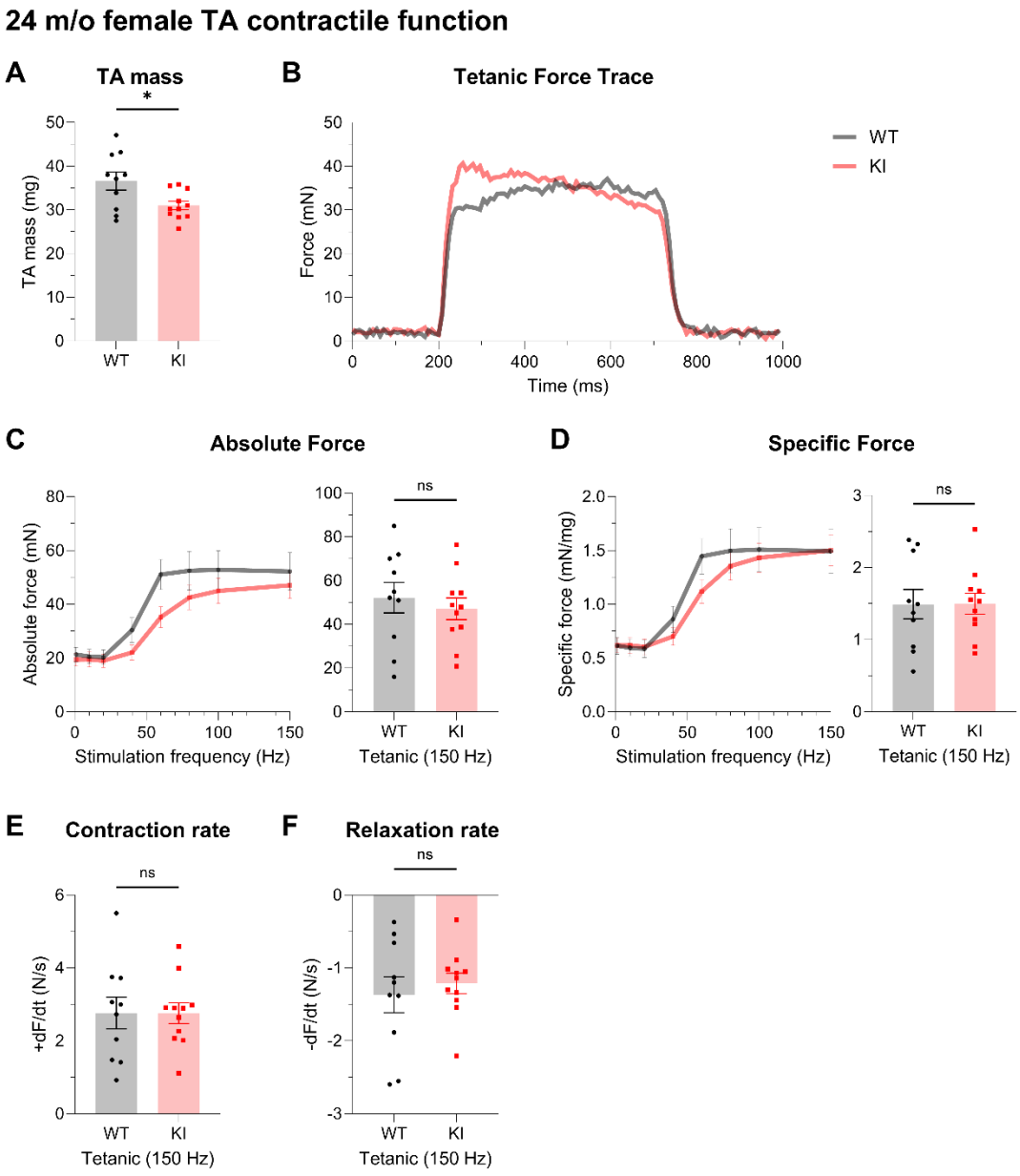

Figure 2. 14 *In vivo* nerve-evoked isometric force measurements in 24-month-old female TA muscle.

Contractility was assessed using *in vivo* nerve-evoked isometric contractions. The common peroneal nerve was percutaneously stimulated by brief (500 msec) trains of pulses delivered at 1 to 150 Hz. Similar to 12-months, at 24-months KI female TA muscles exhibited comparable muscle mass (**A**), absolute tetanic force **(B-C)**, specific force **(D)**, as well as rates of contraction **(E)** and relaxation **(F)** compared to their WT counterparts; *n*=10 WT and *n*=11 KI female mice per genotype. Data is presented as mean ± SEM and statistical significance was determined by 2-tailed Student's *t*-test **(A & E)**, 2-way ANOVA followed by Šidák's test for multiple comparisons **(C & D)**, or Welch's *t*-test **(F)**; ns: not significant.

Collectively, these findings demonstrate a sex-dimorphic manifestation of the E248K Myotrem myopathy in late adulthood with males being more severely affected than females and structural deficits likely driving contractile impairment, consistent with the essential role of sMyBP-C in sarcomeric organization and maintenance (7, 29).

2.3 Discussion

MYBPC1 is an essential sarcomeric gene encoding slow MyBP-C (sMyBP-C) that has both structural and regulatory roles (29). Pathogenic *MYBPC1* variants have been previously associated with the development of severe and lethal forms of arthrogryposis multiplex congenita (5, 12, 28, 40), and more recently with a new form of myopathy, referred to as Myotrem. Myotrem is characterized by early-onset generalized muscle weakness, hypotonia, skeletal deformities manifesting as spinal rigidity and scoliosis, dysmorphia, respiratory deficiencies, and most notably a postural tremor of myogenic origin (14, 15, 19, 21). Identification of Myotrem in the human population occurred in a multigenerational Latvian family heterozygous for the E248K variant, residing in the NH_2-terminal M-motif of the protein that is implicated in the dynamic binding to both myosin and actin filaments (14). The index patient, a 30-year-old man at the time of diagnosis, exhibited the characteristic Myotrem phenotype that peaked in adolescence, reaching a phase of stabilization in early adulthood with no evidence of further deterioration (14). To study the E248K Myotrem myopathy *in vivo*, our group developed the relevant KI murine model. Importantly, the E248K model faithfully recapitulates Myotrem presentation postnatally and in early adulthood (24), establishing it as a reputable proxy to investigate the disease pathogenesis and progression.

Herein we took advantage of the E248K murine model to examine how the E248K Myotrem myopathy progresses through aging and whether it displays a sex-dimorphic manifestation. Notably, while biological variability becomes more conspicuous with age (41), an attribute we also witnessed in the WT group, KI animals displayed minimal intrasubject variability, likely reflecting a consistent (mal)adaptation of muscle structure/function elicited by the myopathy. Our findings reveal that the stabilization phase reached in early adulthood persists in mid adulthood in both sexes. Interestingly though, 12-month-old E248K male TA muscle exhibits a trending structural and contractile decline, in the absence of any changes in the expression levels of sMyBP-C or the DRX:SRX ratio of myosin heads. Conversely, 12-month-old E248K female TA muscle shows no signs of structural or contractile deficits, secondary to an upregulation of sMyBP-C expression at 6-months, possibly an early adaptive response, that reverts to downregulation at 12-months, and an accompanied increase of myosin heads in the DRX state. The apparent lack of structural deficits in E248K female TA muscle at 12-months, albeit the decreased levels of sMyBP-C, suggests that there is a critical amount of sMyBP-C that is sufficient to maintain sarcomeric organization. Consistent with this notion, heterozygous carriers of the p318* nonsense mutation, residing in the NH_2-terminal Ig C2 domain resulting in partial loss of sMyBP-C, are asymptomatic, while homozygous carriers develop Lethal Congenital Contractural Syndrome-4 (LCCS-4) and perinatal lethality (13). Considering the reported role of sMyBP-C in stabilizing the energetically less demanding SRX state of myosin heads (34, 42), it is tempting to speculate that the reduced levels of sMyBP-C in 12-month-old female muscles may underlie the observed upregulation of myosin heads in the DRX state, possibly serving as an adaptive response, to slow contractile decline.

Relatedly, up-regulation of the DRX myosin state was recently reported in nemaline myopathy, possibly as an early compensatory mechanism (43). Thus, although at a gross level, Myotrem myopathy manifests similarly in the two sexes in mid adulthood, distinct alterations appear to take place at the biochemical and cellular levels, likely impacting the progression of the disease in late adulthood.

The trending contractile decline observed in E248K Myotrem male mice in mid adulthood progresses to significant deterioration in late adulthood, independently of the muscle examined, coinciding with prominent structural alterations. This worsening in muscle structure/function is likely aggravated by physiological, age-related changes in muscle architecture (44), further halting the stabilization period. By contrast, muscle structure and contractile performance in E248K Myotrem female mice appears to be preserved at 24-months, with TA muscle showing no structural or functional decline. These intriguing findings raise a major question: what is the basis of the sex-dimorphic, muscle-dependent manifestation of E248K Myotrem (and possibly Myotrem in general) in response to aging?

The highly beneficial effects of estrogen in skeletal muscle structure/function have been extensively documented (45). At the myofilament level, estrogen modulates myosin relaxation kinetics (46, 47) and thus actomyosin contractility (34). Accordingly, estrogen depletion via ovariectomy diminishes the lifetime of SRX myosin heads (46), while estrogen attrition due to aging shortens the lifetime of both SRX and DRX myosin heads (47). At the tissue level, estrogen contributes to muscle mass maintenance (48), improves muscle tone and strength (49, 50), and enhances muscle regeneration and repair in response to injury via satellite cell activation (45, 51). These estrogen-mediated protective effects

are consistent with the lack of contractile decline in the female E248K Myotrem population in late adulthood.

Given the newness of Myotrem as a distinct disease entity, the lack of effective therapies is a major unmet clinical need, as patients are often treated with steroids aiming to improve muscle mass and strength, yet experiencing serious side effects, and β-blockers, commonly used to treat abnormal heart rhythm and hypertension, or primidone, typically used to control epileptic seizures, which however fail to alleviate tremors. Although life expectancy appears not to be affected in E248K Myotrem carriers, skeletal muscle quality and health in late adulthood is of paramount importance when considering factors such as independent walking, physical activity, agility, fall risk, fatigue, and thus overall well-being (52, 53). The surge in reported cases of Myotrem (18-21, 28) since its original identification in 2019 (14, 15), coupled with its non-progressive phenotype from adolescence through mid adulthood, may imply that the actual prevalence of Myotrem is higher than what was originally presumed. Thus, deciphering the disease pathogenesis and presentation as a function of biological sex, muscle type, and aging is imperative for the comprehensive characterization of the disease and the design of effective and targeted therapies.

2.4 Materials and Methods

Our study examined male and female animals and sex-dimorphic effects are reported.

Survival curves: Kaplan-Meier curves were generated for WT and heterozygous KI animals from 4-weeks through 24-months of age. Statistical significance comparing survival rates between WT and KI was performed using the log-rank test.

Inverted hang assay: Mice were placed on a wire grid hung ~50 cm above a soft padded surface. The grid was slowly inverted over a time period of 2 seconds. Hang time was measured as the time from full inversion to until the animal dropped. If the mouse did not fall after 3 minutes, the assay was stopped, and the maximum time of 180 seconds was recorded. The animal was returned to its cage and allowed to rest for at least 3 minutes. The assay was repeated three times in one day. Individual data-points reflect the average of these three trials per animal.

Dual-energy x-ray absorptiometry (DEXA): Animals were lightly anesthetized and exposed to DEXA (iNSiGHT VET DXA, Osteosys, Seoul, South Korea) scans. For body composition measurements, the animals were placed in a prone position during the scan. A region of interest (ROI) of the animal body excluding the head and tail was used for estimations of total mass, lean mass, and fat mass. For spinal curvature measurements, the animal was placed in a right lateral recumbent position during the scan. Kyphotic index was determined as previously described (24, 54) by calculating the ratio of the distance between the C7 and L6 vertebrae and the length of a perpendicular line reaching the extreme dorsal curvature of the spine.

Immunofluorescence combined with confocal microscopy and image processing: Mice were deeply anesthetized and perfused with 4% paraformaldehyde in PBS. The TA muscle was rapidly harvested and embedded in Tissue-Tek OCT Compound (Sakura, Osaka, Japan). 10 μm thick cryosections were cut, permeabilized with 0.1% Triton-X in PBS for

20 minutes and blocked with 2% goat serum, 2% BSA, 1 mM NaN3 in PBS for 30 minutes at room temperature. Tissue sections were labeled with primary antibodies against sarcomeric α-actinin (mouse monoclonal, Sigma-Aldrich, A7811, 1:1000, Millipore Sigma, St. Louis, MO) and sMyBP-C (rabbit polyclonal, Sigma-Aldrich, SAB3501005, 1:250, Millipore Sigma, St. Louis, MO). Samples were counterstained with the appropriate fluorophore-conjugated secondary antibody (Alexa Fluor 488 or Alexa Fluor 568, Invitrogen, A11034 or A21043, 1:250, Thermo Fisher, Waltham, MA) along with Hoescht 33258 dye (Thermo Fisher Scientific, Waltham, MA), and subsequently mounted with ProLong Diamond Antifade Mountant (Thermo Fisher Scientific, Waltham, MA). Slides were imaged using a Nikon Ti2 inverted spinning disk confocal microscope and images were taken at 60x magnification. Five representative ROIs from a total of three biological samples per sex/per genotype/per age were analyzed. Images were compiled into a z-stack, processed, and quantitatively analyzed for sarcomeric structural organization and sMyBP-C localization using FIJI software (NIH, Bethesda, MD).

Quantification of sarcomeric organization and sMyBP-C localization: Tissue sections immunostained for α-actinin were used to calculate sarcomeric breakage, continuity, and order scores. In particular, images underwent skeletonization and branching analysis using the Skeletonize3D and AnalyzeSkeleton FIJI plugins. The number and length of branches were used to calculate the "breakage" and "continuity" scores, respectively. Moreover, α-actinin stained images were subjected to Fast Fourier Transform (FFT) analysis to determine the sarcomeric "order" score based on the regularity of Z-disk periodicity, as previously described (55). The resulting power spectra were analyzed using a customized

Python script (https://github.com/humbertojoca/FFT_peaks) that calculated the relationship of intensity *versus* spatial frequency. The first peak, located at ~0.4 μm^{-1} on the power spectrum **(Fig. 2.3 B' and E'**; **green arrow),** and the corresponding peak in the resulting trace **(Fig. 2.3 B" and E"; marked in green)**, reflect sarcomeric "order". The amplitude of the first peak was reported as the "order" score.

The breakage, continuity, and order scores were then collectively used to classify the type of sarcomeric (dis)organization shown in Supplemental Fig. 3, as: "prototypic sarcomeric organization" characterized by a regular striated pattern **(Fig. 2.4 A)**; "lateral misalignment" characterized by lateral dissociation of adjacent myofibrils **(Fig. 2.4 B)**; "sarcomeric continuum" characterized by uninterrupted wavy-like striations **(Fig. 2.4 C)**; "disordered organization" characterized by irregular and out-of-register sarcomeres in the absence of lateral breakage **(Fig. 2.4 D)**; and "chaotic organization" characterized by irregular and out-of-register sarcomeres in the presence of lateral breakage **(Fig. 2.4 E)**.

The localization of sMyBP-C to the C-zone in its characteristic doublet was evaluated using two methods. The first method qualitatively evaluated sMyBP-C distribution along a ~10 μm ROI using FIJI. Specifically, normalized signal intensity values of α-actinin (marker of overall sarcomeric structure) and sMyBP-C were plotted *versus* distance along the ROI to visualize their striated localization patterns. The second method quantitatively evaluated sMyBP-C localization throughout the entire image. sMyBP-C-stained images underwent FFT analysis, as described in (55). The resulting power spectra were analyzed using a customized Python script (https://github.com/humbertojoca/FFT_peaks), and the intensity

versus spatial frequency was plotted. The second peak, located at ~0.8 μm^{-1} on the power spectrum **(Supplemental Fig. 2.3 C' and F'; red arrow)**, and the corresponding trace **(Supplemental Fig. 2.3 C" and F"; marked in red)**, reflect sMyBP-C localization to the C-zone. The amplitude of the second peak was reported as the sMyBP-C "localization" score.

Generation of protein lysates and immunoblotting: Freshly isolated TA muscles were harvested from 12- and 24-month-old mice using flash frozen liquid nitrogen. A small (~15 mg) portion of the mid-belly of the muscle was sampled for lysate generation via hand-homogenization in a modified NP-40 lysis buffer (10 mM NaH_2PO4, pH 7.2, 2 mM EDTA, 10 mM NaN_3, 120 mM NaCl, 0.5% deoxycholate, 1% NP-40) supplemented with cOmplete protease inhibitor (Roche, Indianapolis, IN) and Halt phosphatase inhibitor (Thermo Scientific, Waltham, MA) cocktails. NuPage LDS sample buffer and reducing agent (Invitrogen, Waltham, MA) were added to 20 µg of protein lysates, boiled at 95° C for 5 minutes, and fractionated by 4-12% SDS-PAGE. Protein was transferred to nitrocellulose membrane, and blocked with 5% milk (RPI, Mt Prospect, IL) in Tris Buffered Saline containing 0.1% Tween-20. Blot strips were then probed with antibodies against sMyBP-C (rabbit polyclonal, Sigma-Aldrich, SAB3501005, 1:12000, Millipore Sigma, St. Louis, MO) or GAPDH (mouse monoclonal, Sigma-Aldrich, G8795, 1:30000, Millipore Sigma, St. Louis, MO) at 4°C overnight. Blots were subsequently incubated in the appropriate horseradish peroxidase-conjugated secondary antibody (Cell Signaling Technology, Danvers, MA) and ECL substrate (Thermo Scientific, Waltham, MA).

Densitometry was performed with ImageJ software (NIH, Bethesda, MD) and the average value of two technical replicates were used for analysis.

***In vivo* assessment of TA function**: In vaporized isoflurane-anesthetized mice, the hindlimb was immobilized at the knee and the foot was secured to a force transducer (1300A, Aurora Scientific, Aurora, ON, Canada). The common peroneal nerve was then stimulated with brief (500 msec) trains of pulses delivered at 1 to 150 Hz to elicit isometric contractions of the TA muscle and the resulting force was measured. The data were plotted to display the prototypic force-frequency relationship, and the tetanic measurements delivered at 150 Hz were used as outcome variables. Specific force was calculated by dividing the absolute peak force measurement by the mass of the isolated muscle.

Single nucleotide turnover Mant-ATP assay: Biochemical assessment of the myosin relaxation states was determined using single nucleotide turnover Mant-ATP chase experiments, as previously reported (43). In short, mice were humanely euthanized via CO_2 inhalation followed by cervical dislocation. The TA muscle was quickly harvested and placed in a skinning solution of 1:1 glycerol to relaxing solution containing 4 mM Mg-ATP, 1 mM free Mg^{2+}, 10^{-6} mM free Ca^{2+}, 20 mM imidazole, 7 mM EGTA, 14.5 mM creatine phosphate and KCl to adjust the ionic strength to 180 mM and the pH to 7.0. The tissue was pinned on Sylgard plates to maintain its resting length, incubated in relaxing solution at -20°C for 48 hours, and subsequently cryopreserved at -80°C until experimentation.

On the day of experimentation, bundles were thawed, single myofibers were mechanically isolated and mounted inside a flow chamber at a resting sarcomere length of ~2.20 μm. Fibers were incubated with rigor buffer, containing 120 mM K acetate, 5 mM Mg acetate, 2.5 mM K2HPO4, 50 mM MOPS, 2 mM DTT, pH 6.5, for 5 minutes. The flow chamber was then flushed with rigor buffer containing 250 μM Mant-ATP and allowed to incubate for 5 minutes. To complete the chase, the flow chamber was subsequently flushed with rigor buffer containing 4 mM unlabeled ATP. Florescence was acquired using a Zeiss Axio Scope A1 microscope and three ROIs per myofiber were used for analysis. Normalized florescence intensity signals were fit to an unconstrained double exponential decay curve using GraphPad Prism (GraphPad Software, Boston, MA): $Normalized\ Fluorescence = 1 - P_1(1 - exp^{\left(-\frac{t}{T_1}\right)} - P_2(1 - exp^{(-\frac{t}{T_2})}$, where the initial rapid decay corresponds to the disordered-relaxed (DRX) state and the slower second decay corresponds to the super-relaxed (SRX) state of myosin heads. P_1 and P_2 represent the respective amplitudes while T_1 and T_2 denote the respective time constants.

Statistical analyses: Statistical tests, sample sizes (*n*), and *p* values are provided in figure legends. Data are presented as mean ± SEM and were analyzed by GraphPad Prism (San Diego, CA). The D'Agostino & Pearson test was used to examine normality and an F test was used to compare variances. Comparisons between two normal datasets of similar variance were performed using Student's 2-tailed *t*-test. Mann-Whitney test or Welch's *t*-test was used for datasets that failed the normality or variance test, respectively. Force-frequency plots were analyzed with 2-way ANOVA followed by Šidák's test for multiple

comparisons. Values are expressed as mean ± SEM; *p<0.05, **p<0.01, ***p<0.001, and ****p<0.0001.

Study approval: All animal work was conducted under protocols approved by the Institutional Animal Care and Use Committee of the University of Maryland School of Medicine. Studies use 6-, 12- and 24-month-old WT and heterozygous E248K KI C57BL/6J mice. Generation of the KI murine model was previously described in (24) and contains the murine *Mybpc1* E249K substitution corresponding to the human E248K variant. KI mice are referred to as the *MYBPC1* E248K KI murine model to avoid confusion. The model is maintained with regular backcrossing to avoid genetic drifting and off-target effects.

Data availability: The graphical abstract was prepared with BioRender under the agreement number: HW26QVMKZV.

CHAPTER 3

Pulsatile activity in the E248K Myotrem murine model: Putative pacemaker myofibers initiate myogenic tremor

This chapter outlines a short work submitted to American Journal of Physiology: Cell Physiology. I served as co-first author and contributed to conceptualization, data analysis, interpretation of results, figure preparation, and manuscript writing. This study is performed in collaboration with the McDonald Lab which performed all biomechanical measurements with work from Dr. Kerry McDonald, PhD, who serves as co-corresponding author, and Dr. Laurin Hanft, who serves as co-first author.

3.1 Introduction

Pathogenic variants in *MYBPC1*, the gene encoding the slow skeletal isoform of Myosin Binding Protein-C (sMyBP-C), are linked to a newly recognized form of congenital myopathy termed Myotrem (OMIM #618524), characterized by congenital hypotonia, early onset muscle weakness, skeletal deformities, and, most characteristically, tremor of myogenic origin (14). The myogenic tremor is largely postural, accentuated with action, and is present mainly in the upper and lower extremities as well as the tongue (14). sMyBP-C is ubiquitously expressed in skeletal muscle in both slow- and fast-twitch fibers, although in different amounts and isoform combinations (9). Localized to the C-zone of the sarcomeric A-band (56), sMyBP-C is constitutively bound to the thick filament at its COOH-terminal end (57), while its NH_2-terminus interacts dynamically with both myosin (23) and actin (22, 58). sMyBP-C plays a role in the assembly and maintenance of

sarcomeric organization (6) and critically regulates actomyosin crossbridge cycling. Given that sMyBP-C expression is restricted to skeletal muscle and that Myotrem patients exhibit no neuropathy, the tremor is believed to originate in the muscle itself starting at the level of the sarcomere (14). However, the molecular mechanism(s) of myogenic tremorgenesis is unknown.

Stretch activation is a property of striated muscle whereby rapid mechanical stretch of an isolated muscle fiber leads to a delayed increase in force (59, 60). This stretch-activated response occurs in three phases. In *phase 1*, mechanical stretch strains actomyosin crossbridges, generating a rapid increase in tension. In *phase 2,* tension rapidly decreases as strained crossbridges detach. Finally, in *phase 3*, there is a slow increase in muscle tension, known as stretch activation. Stretch activation is most apparent in an opposing pair of indirect flight muscles (IFM) in insect species, such as Drosophila (61, 62), where the contraction of an agonist muscle leads to the coincident stretch of the antagonist muscle. This initiates a stretch-activated contraction in the antagonist muscle, and a simultaneous stretch of the agonist muscle. This feedback loop allows for cyclical stretch and contraction of the IFM pair, propagated predominately by mechanical stretch, not electrical or Ca^{2+} signals (60). Free from the constraints of Ca^{2+} ion diffusion, stretch-activated contraction occurs more rapidly than membrane depolarization, and is thus referred to as "asynchronous contraction" (63).

Although more pronounced in IFM, stretch activation is a property of vertebrae striated muscles as well and contributes to physiological function (59, 64). For example, in cardiac myocytes, which rhythmically contract with each heartbeat, stretch activation is thought to contribute to length-dependent activation and the Frank-Starling mechanism (65).

Although the mechanisms of stretch activation are not fully understood, alterations in the levels or phosphorylation status of MyBP-C have been shown to regulate stretch activation in cardiac myocytes (66) and skeletal muscle fibers (67).

In this study, we use a murine model harboring the dominant *MYBPC1* E248K substitution, to understand stretch activation in the predominantly slow-twitch soleus muscle. Our findings indicate that a subpopulation of permeabilized E248K soleus fibers exhibit a persistent and regular unsolicited pulsatile phenotype, when placed in a submaximal Ca^{2+} activating solution. Further analysis shows that these pulsing fibers are immuno-positive for the slow myosin heavy chain isoform and display enhanced stretch activation properties in comparison to wild-type (WT) and non-pulsing E248K knock-in (KI) fibers. Taken together, we report novel evidence of intrinsic contractile activity in a population of isolated Myotrem slow-twitch fibers and provide putative mechanistic insights for myogenic tremorgenesis.

3.2 Materials and Methods

Study approval: All animal work was conducted under protocols approved by the Institutional Animal Care and Use Committee of the University of Maryland School of Medicine. Studies use 2-month-old WT and heterozygous E248K KI male mice. The generation of the Myotrem murine model was previously described (24), expressing the murine *Mybpc1* E249K substitution corresponding to the human E248K variant. KI Myotrem mice are referred to as the *MYBPC1* E248K KI murine model to avoid confusion. To maximize consistency, this study focuses on measurements from male mice, as many neuromuscular disorders are known to affect males and females differently (68).

Solutions: Relaxing solution consisted of 1 mM dithiothreitol (DTT), 100 mM KCl, 10 mM imidazole, 2.0 mM EGTA, 4.0 mM ATP, and 1 mM free (5 mM total) $MgCl_2$, supplemented with Pefabloc protease inhibitor (Supelco, MilliporeSigma, Burlington, MA, USA). Basal Ca^{2+} activating solution contained 7.00 mM EGTA, 20 mM imidazole, and 14.50 mM PCr. Minimal Ca^{2+} activating solution (pCa 9.0) was supplemented with 5.42 mM $MgCl_2$, 72.37 mM KCl, 0.016 mM $CaCl_2$, and 4.7 mM ATP. Maximal Ca^{2+} activating solution (pCa 4.5) was supplemented with 5.26 mM $MgCl_2$, 60.25 mM KCl, 7.01 mM $CaCl_2$, and 4.81 mM ATP. Submaximal activating solutions of intermediate pCa values ranging between 5.9 and 6.5 were made by combining the appropriate ratios of minimal and maximal Ca^{2+} solutions.

Fiber preparation and experimental setup: Fiber preparation, experimental setup, stretch-activated force measurements, and data analysis occurred as described previously (67). In short, mice were euthanized via asphyxiation using carbon dioxide followed by cervical dislocation. Soleus muscle was isolated and secured at each tendon to a toothpick to preserve sarcomere length. The tissue was incubated in a 1:1 relaxing solution:glycerol at -20 °C to allow for chemical skinning. On the day of experimentation, single fibers were dissected, and the ends of the fiber were secured to stainless steel troughs with 3-0 monofilament sutures and subsequently mounted to a capacitance gauge force transducer (model 403, sensitivity of 20 mV/mg, resonant frequency of 600 Hz; Aurora Scientific) and a length control fitted to a DC torque motor (model 308c; Aurora Scientific). The apparatus was mounted over an Olympus IX70 inverted florescent microscope on a

pneumatic vibration isolation table. Morphological measurements were made while the fiber preparation was relaxed. Sarcomere length was monitored continuously using the IonOptix SarcLen video system and fast Fourier transform analysis of a ~220 x 30 μm region of interest and all measurements were performed at 15°C ± 1°C. A total of 8 fibers from 5 WT mice and 11 fibers from 5 KI mice were harvested for experimentation.

Slack-restretch protocol: Slack-restretch experiments were performed as described previously (67, 69) to measure crossbridge kinetics in maximal Ca^{2+} activating conditions (pCa 4.5). In brief, permeabilized fibers were placed in maximal Ca^{2+} activating solution (pCa 4.5) at optimal length and steady state was allowed to develop. Subsequently, the fiber was slackened, rapidly re-stretched to mechanically detach cross-bridges to a value slightly greater than optimal length for ~2 ms, and returned to optimal muscle length allowing for crossbridge formation and force redevelopment. The resulting force curve was fit to a single exponential equation: $F = F_{res} + F_{max}(1 - e^{(-k_{tr})x}$, where the force, F, at any time x, is related to the residual tension immediately after the slack-restretch maneuver (F_{res}), the maximal force (F_{max}), and the rate constant of force development, (k_{tr}). For each fiber, the slack-restretch maneuver was performed at the onset and conclusion of the biomechanical protocols and the reported k_{tr} value is the average of these two repeats.

Step-stretch protocol and data analysis: Following the initial slack-restretch protocol, the fiber was transferred to submaximal Ca^{2+} activating solution and subjected to a step-stretch protocol to investigate stretch activation properties. The fiber was allowed to reach steady-state tension (P_O), and then rapidly stretched 1% of the initial sarcomere length.

This stretch elicited changes in force that exhibited the prototypical triphasic stretch-activated response: immediate sharp increase in force (P_1) *in phase 1*; subsequent decrease in force (P_2) *in phase 2*, that occurs with a kinetic constant of k_{rel}; and stretch activation *in phase 3*, which is the slow delayed development in force (P_{TO}) following stretch that occurs at a time constant of k_{df}. The force trace during this phase was fit to a "single exponential rise to maximum" equation: $F = P_2 + P_{TO}(1 - e^{(-k_{df})x}$ whereby F is the force at x seconds of *phase 3*. The fiber then reached a new steady state tension (P_{SS}). This stretch was held for about 6 sec before the fiber was shortened to its original sarcomere length. The fiber was allowed to reach steady-state tension again at this original length before undergoing subsequent step stretches at ~2%, ~3%, and ~4% sarcomere length, and the stretch-activated response of each stretch was recorded. For each fiber, this protocol was repeated in two different submaximal Ca^{2+} solutions: one that elicited ~50% of the fiber's maximal Ca^{2+} activated force (pCa where $P_O/P_{pCa4.5}$=50%), and a second which elicited ~25% of the fiber's maximal Ca^{2+} activated force (pCa where $P_O/P_{pCa4.5}$=25%). Stretch activation tension measurements, such as *phase 1* maximum force (P_1), *phase 2* minimum force (P_2), stretch-activated force development (P_{TO}), and stretch-induced steady state force (P_{SS}) were normalized to the initial steady state force (P_O). Stretches that did not elicit a stretch-activated response (P_{TO}=0) were excluded from final analysis. Percent stretch (1-4%) and submaximal pCa ($P_0/P_{pCa4.5}$=25% and $P_O/P_{pCa4.5}$=50%) did not vary significantly between experiments and thus all stretch-activated responses were pooled for analysis.

Single fiber immunoblot analysis: Following mechanical measurements, single permeabilized fibers were incubated in relaxing solution with sodium dodecyl sulfate

(SDS). Individual fibers were fractionated by SDS-PAGE using a 4-12% tris-acetate gel (Invitrogen, Waltham, MA, USA) and transferred to nitrocellulose membrane. Lysates from whole soleus WT and KI muscles were included as positive controls and total protein was visualized using SYPRO Ruby protein staining (Thermo Scientific, Waltham, MA). The blot was subsequently cut into strips and probed with antibodies against the slow isoform of myosin heavy chain (mouse monoclonal, Sigma-Aldrich, M8421, 1:1000, Millipore Sigma, St. Louis, MO, USA) and sMyBP-C (rabbit polyclonal, Sigma-Aldrich, SAB3501005, 1:1000, Millipore Sigma, St. Louis, MO, USA) at 4° C overnight. After washing, the strips were incubated with the appropriate horseradish peroxidase-conjugated secondary conjugated secondary antibody (Cell Signaling Technology, Danvers, MA) and subsequent ECL substrate (Thermo Scientific, Waltham, MA). Poorly preserved fibers were excluded from analysis and thus reported immunoblot data reflects 7 of 8 WT fibers, 6 of 8 quiescent KI fibers, and 3 of 3 pulsing KI fibers.

Statistical analysis: Statistical tests, sample sizes (n), and p-values are provided in figure legends. Comparisons between WT, KI quiescent, and KI pulsing groups were performed using one-way ANOVA and were analyzed by GraphPad Prism (San Diego, CA). Differences in variances amongst the groups were assessed using Bartlett's test. Ordinary ANOVA followed by Tukey's test for multiple comparisons or Brown-Forsythe and Welch ANOVA followed by Dunnett's T3 test for multiple comparisons was used to compare homoscedastic or heteroscedastic datasets, respectively. Values are expressed as mean ± SEM; ns: not significant, *p<0.05, **p<0.01, ***p<0.001, and ****p<0.0001.

3.3 Results

3.3.1 Pulsative activity of a subpopulation of skinned KI Myotrem soleus fibers

Permeabilized soleus fibers were isolated from WT and KI *MYBPC1* E248K Myotrem mice and subjected to biomechanical measurements in submaximal Ca^{2+} conditions. All 8 WT fibers and 8 of 11 isolated KI fibers remained at constant sarcomere length during sub-maximal Ca^{2+} activation consistent with prototypic behavior **(Figure 3.1 A-B)**. Remarkably however, a subpopulation of 3 of 11 (27%) KI fibers exhibited pulsatile activity **(Figure 3.1 C)** during sub-maximal Ca^{2+} activation. This pulse behavior consisted of autonomous contraction and relaxation cycles throughout the length of the fiber, unremitting on a time scale of minutes, and present despite subsequent small rapid mechanical stretches. Hereby, we will be referring to the subpopulation of KI fibers that exhibit unsolicited contractile behavior as pulsing to be distinguished from quiescent KI fibers.

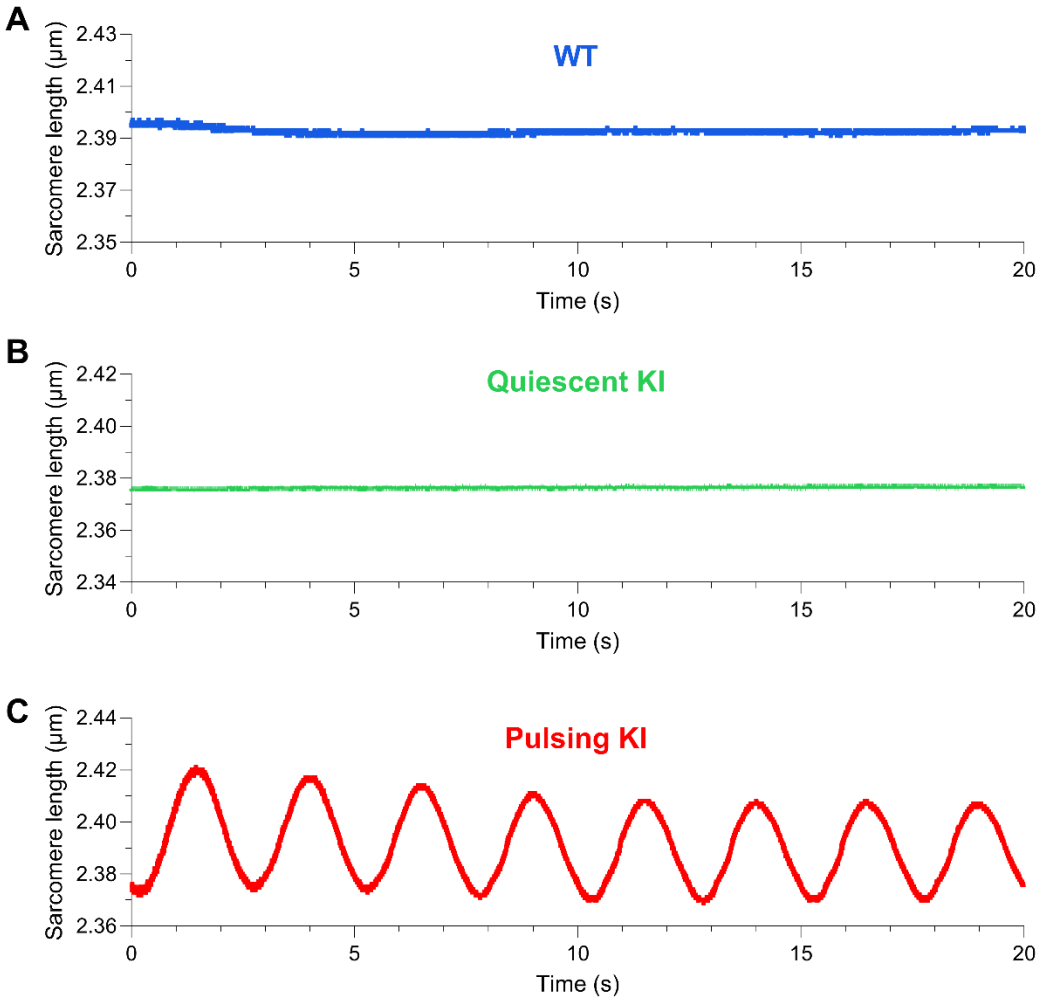

Figure 3. 1 A small population of skinned KI fibers show pulsatile activity.
Soleus fibers from 2-month-old male mice were chemically skinned, mechanically isolated, attached to a length controller and force transducer to either end, and submerged in a relaxing solution of submaximal Ca^{2+} concentration (WT, pCa 6.0; quiescent KI, pCa 6.2; pulsing KI, pCa 6.2). Fiber length was kept constant, and sarcomere length was measured using the IonOptix SarcLen system and Fast Fourier Transform (FFT) analyzing a ~200 x 30 µm region of interest. Representative WT **(A)** and quiescent KI **(B)** fibers remained at a constant sarcomere length, while a small population of KI fibers showed a "pulsing" phenotype **(C)**. Data shown are over a 20 sec period of steady-state equilibrium with a sampling rate of 250 Hz.

Sarcomere length traces of these pulsing KI fibers revealed a unique sinusoidal pattern with temporally equivalent lengthening and shortening phases, reaching a consistent amplitude with each period **(Figure 3.1 C)**. Despite this internal consistency, amplitude and frequency values varied amongst the three (3) KI fibers exhibiting pulse

(Figure 3.2). Pulse amplitude and frequency also changed within the same fiber in a pCa-dependent manner, where lower Ca^{2+} concentrations dampened pulse amplitude and frequency **(Figure 3.2)**. Pulsing behavior was only apparent in solutions with submaximal Ca^{2+} levels and was not observed in relaxing solution (no Ca^{2+}), where the relaxed fiber remained static, or in maximal Ca^{2+} activating solution (pCa 4.5), where the fiber contracted uniformly, in prototypic fashion.

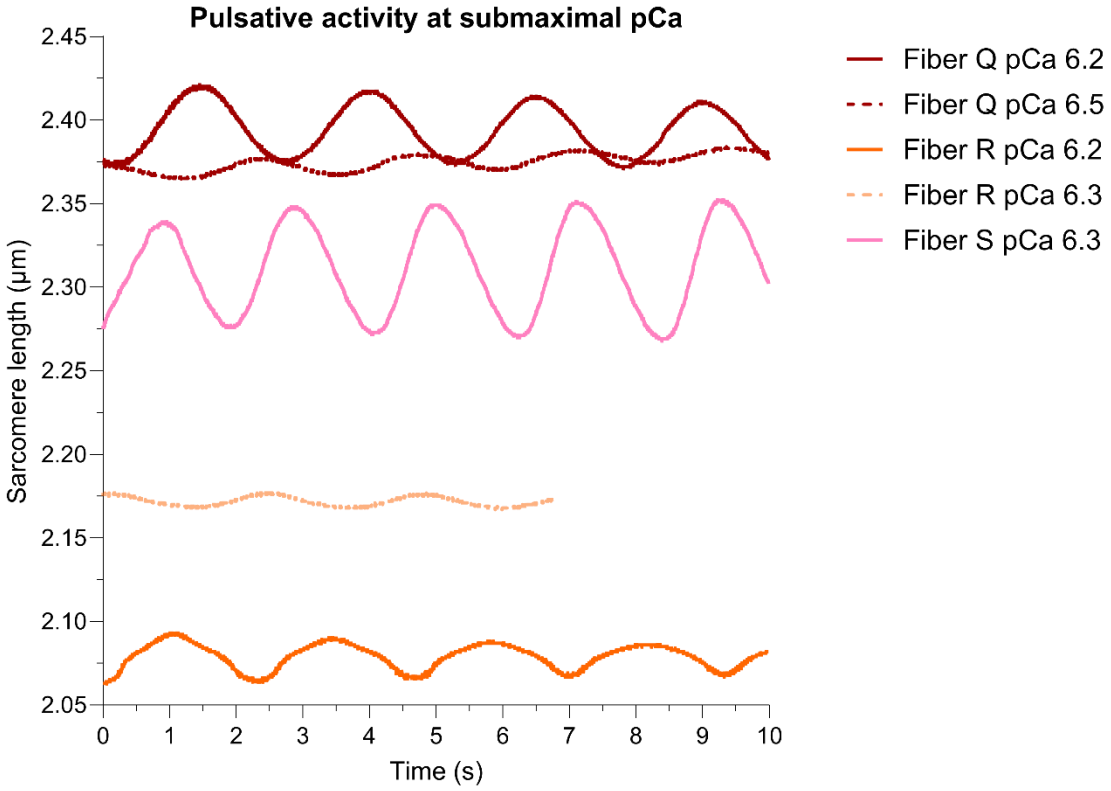

Figure 3. 2 Pulsatile activity in sarcomere length traces of a subpopulation of KI fibers in submaximal Ca2+ solutions.
Sarcomere length traces of permeabilized KI fibers that show pulsatile activity in submaximal Ca^{2+} solutions (pCa 6.2-6.5). *n*=3 pulsing soleus fibers from *n'*=3 KI mice. Data shown are over a 10 sec period of steady-state equilibrium with a sampling rate of 250 Hz.

3.3.2 Fiber type, cellular characteristics, and contractile function in maximal Ca^{2+} activating solution

We then sought to investigate differences between WT, pulsing KI, and quiescent KI subpopulations to investigate potential mechanisms that qualify KI fibers to exhibit pulsatile behavior. Soleus fibers underwent immunoblot analysis to determine fiber type, by probing for the slow isoform of myosin heavy chain (MHC) and sMyBP-C **(Figure 3.3 A)**. SYPRO Ruby stain was used to evaluate total protein levels in the tested fibers. Interestingly, the three (3) pulsing KI fibers (100%) were positive for myosin heavy chain (MHC)-slow, indicating that they are type-I, slow fibers. Notably, 1 of 6 quiescent KI fibers was also type-I, suggesting that a slow fiber type may be necessary but not sufficient for a KI fiber to elicit pulsatile behavior.

Figure 3. 3 Cellular characteristics of WT, quiescent KI, and pulsing KI fibers are comparable.
(A) WT (lanes A-D and E-G), quiescent KI (lanes I-K and L-N), and pulsing KI (lanes Q, R, S) individual fibers were incubated in SDS buffer and separated by gel electrophoresis. Lysates from whole soleus muscle from WT and KI mice were included as a positive control. SYPRO Ruby was used to visualize total protein levels. Blots were probed for the slow-MHC and sMyBP-C. Slow-MHC was positively identified in 29% WT, 17% quiescent KI, and 100% pulsing KI fibers. n=7 fibers from n'=5 WT mice and n=6 quiescent and n=3 pulsing fibers from n'=5 KI mice. **(B-D)** Morphometric analysis of skinned fibers in relaxing solution revealed no statistically significant differences in total fiber length **(B)**, width **(C)**, and sarcomere length **(D)**. **(E)** The level of passive tension exerted by WT, quiescent KI, and pulsing KI fibers in relaxing solution was similar. **(F)** WT and pulsing KI fibers developed similar maximal tension in maximal Ca^{2+} activating solution, while quiescent KI fibers exerted less tension than WT. **(G)** The tension redevelopment rate was comparable among all three groups. n=8 fibers from n'=5 WT mice and n=8 quiescent and n=3 pulsing fibers from n'=5 KI mice. Data is presented as mean ± SEM and statistical significance was determined by Ordinary ANOVA followed by Tukey's test for multiple comparisons. Values are expressed as mean ± SEM; ns: not significant, $^{**}p<0.01$.

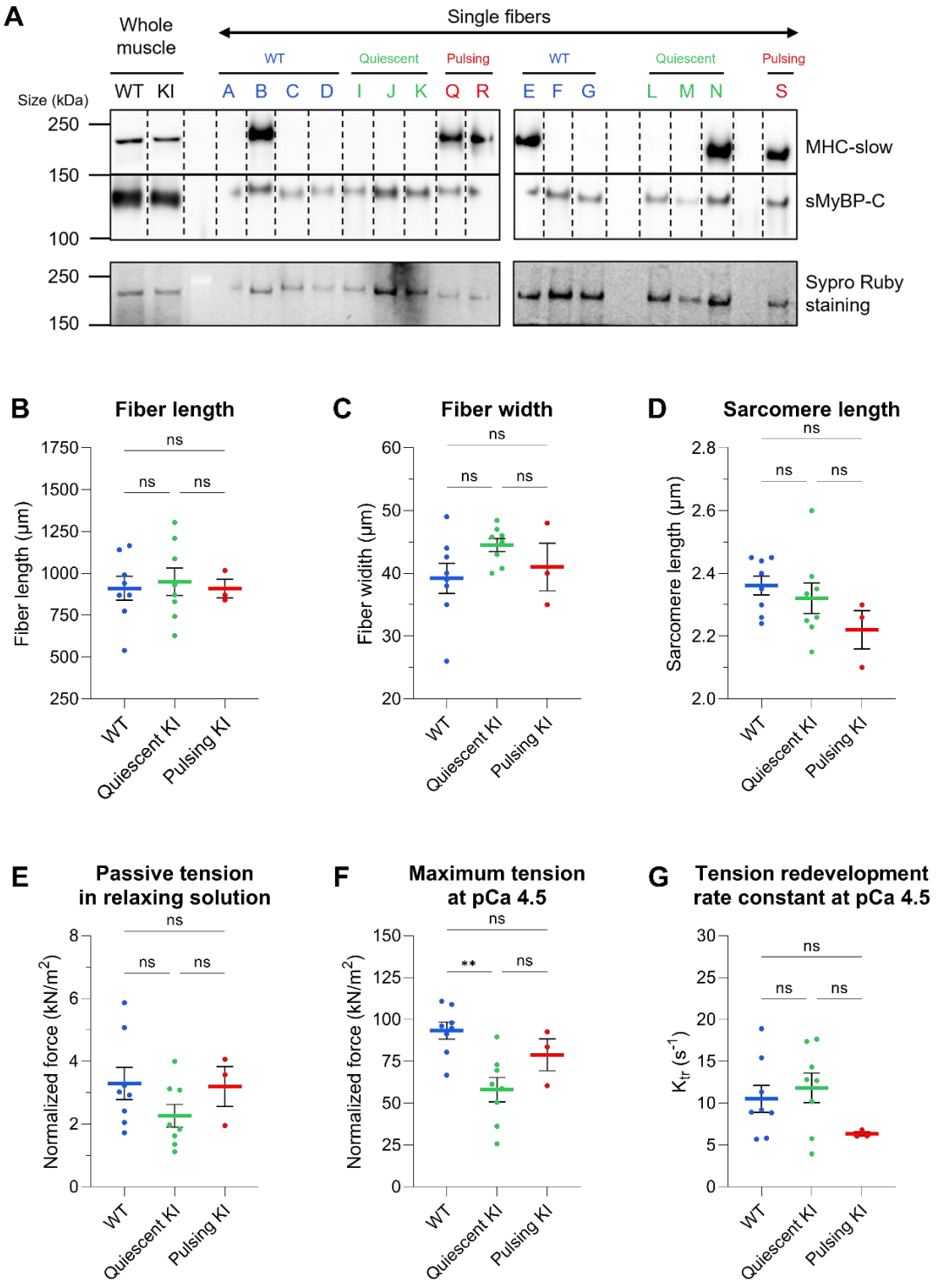
A
Whole muscle
Single fibers
WT
Quiescent
Pulsing
WT
Quiescent
Pulsing
WT KI
A B C D I J K Q R E F G L M N S
Size (kDa)
250
150
100
250
150
MHC-slow
sMyBP-C
Sypro Ruby staining
B
Fiber length
Fiber length (µm)
C
Fiber width
Fiber width (µm)
D
Sarcomere length
Sarcomere length (µm)
E
Passive tension in relaxing solution
Normalized force (kN/m2)
F
Maximum tension at pCa 4.5
Normalized force (kN/m2)
G
Tension redevelopment rate constant at pCa 4.5
Ktr (s-1)
ns
**
WT
Quiescent KI
Pulsing KI

Morphometric measurements in relaxed conditions revealed no apparent differences in terms of total fiber length **(Figure 3.3 B)**, fiber width **(Figure 3.3 C)**, or sarcomere length **(Figure 3.3 D)** between WT, quiescent KI, and pulsing KI fibers. Furthermore, passive tension in relaxing solution did not differ among the three (3) groups **(Figure 3.3 E)**. However, in maximal Ca^{2+} activating solution, quiescent KI fibers exhibited markedly lower maximal tension than WT **(Figure 3.3 F)**. The rate of tension redevelopment did not differ significantly between the three (3) groups but trended to be slower in pulsing KI fibers **(Figure 3.3 G)**, consistent with their MHC content. Collectively, these findings reveal trending biochemical, morphometric, and mechanical properties that generally characterize these populations, but cannot independently predict pulsatile behavior.

3.3.3 Stretch activation properties

Figure 3. 4 Pulsing KI fibers exhibit enhanced stretch activation in comparison to WT and quiescent KI fibers.
(A-C) Representative relative sarcomere length and relative force traces of WT **(A)**, quiescent KI **(B)**, and pulsing KI **(C)** fibers undergoing the step-stretch protocol at 1% sarcomere length stretch in submaximal Ca^{2+} solution (pCa 6.0) exhibiting the prototypic stretch-activated response. Boxed areas of force traces indicate the stretch-activated response and are magnified in the accompanying panels **(A', B', & C')** indicating resting force (P_O), *phase 1* maximum force (P_1), *phase 2* minimum force (P_2), stretch activation (P_{TO}), and stretch-induced steady state force (P_{SS}). Traces for sarcomere length and force represent measurements collected with a sampling rate of 200 Hz and 1000 Hz, respectively. Stretch activation properties were graphed where each point represents a stretch. Stretches that did not induce a stretch-activated response (P_{TO}=0) were excluded from final analysis. **(D)** The rate of delayed force development (k_{df}) trended to be slower in pulsing KI fibers than WT, reaching statistical significance when compared to quiescent KI fibers. **(E)** Stretch activation (P_{TO}/P_O) defined as the force developed during *phase 3* of the stretch-activated response, was greatly enhanced in pulsing KI fibers when compared to both WT and quiescent KI fibers. n=14 stretches of n'=4 fibers from n''=3 WT mice; and n=31 stretches of n'=7 quiescent fibers and n=11 stretches of n'=3 pulsing fibers from a total of n''=5 KI mice. Data is presented as mean ± SEM and statistical significance was determined by Brown-Forsythe and Welch ANOVA followed by Dunnett's T3 test for multiple comparisons **(D),** and ordinary one-way ANOVA followed by Tukey's test for multiple comparisons **(E)**; ns: not significant, *p<0.05, and ****p<0.0001.

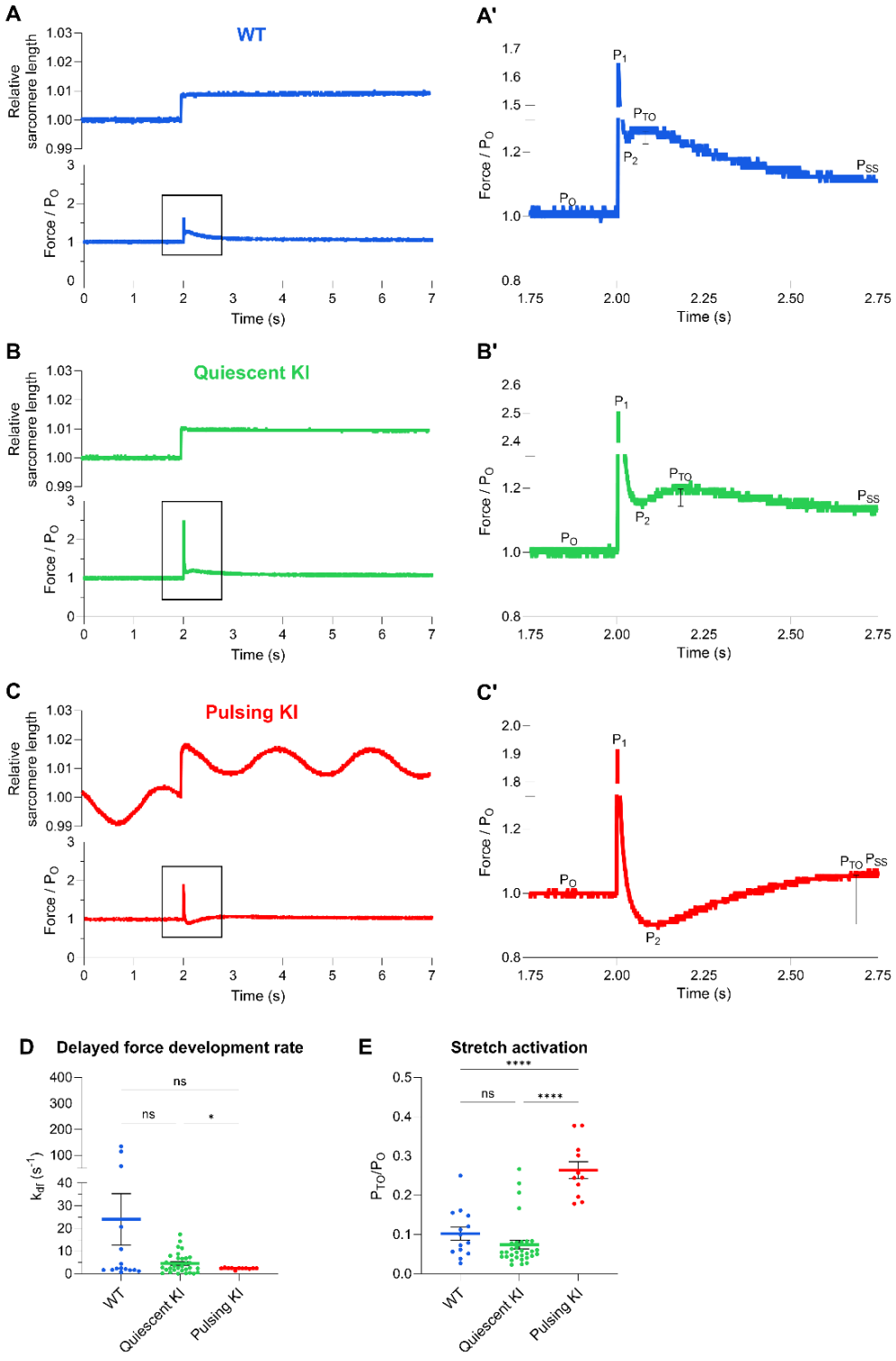
A
WT
Relative sarcomere length
Force / P_O
Time (s)
A'
P_1
P_TO
P_2
P_SS
P_O
B
Quiescent KI
B'
C
Pulsing KI
C'
D
Delayed force development rate
k_df (s^-1)
ns
*
WT
Quiescent KI
Pulsing KI
E
Stretch activation
P_TO/P_O
****

We next investigated stretch activation as a possible mechanism underlying pulsatile activity. Fibers were subjected to rapid step-stretches of 1-4% sarcomere length in submaximal Ca^{2+} conditions (pCa 5.9 to 6.5) and the resulting triphasic step-activated response was recorded **(Figure 3.4 A-C')**. The stretch-activation parameters of each step were evaluated and compared among WT, quiescent KI, and pulsing KI fibers. Pre-stretch tension **(Figure 3.5 A-B),** post-stretch steady-state tension **(Figure 3.5 C)**, and rapid force decay rates (k_{rel}) **(Figure 3.5 D)** were comparable among all three groups. While P_1 force was markedly lower in WT and pulsing KI fibers compared to quiescent KI fibers **(Supplemental Figure 2E)**, P_2 force was substantially decreased in pulsing KI fibers compared to WT and quiescent KI fibers **(Figure 3.5 F)**. Moreover, the rate of delayed force development (k_{df}) was not statistically different between WT and quiescent KI fibers, but it was significantly reduced in pulsing KI fibers compared to quiescent KI fibers **(Figure 3.4 D)**.

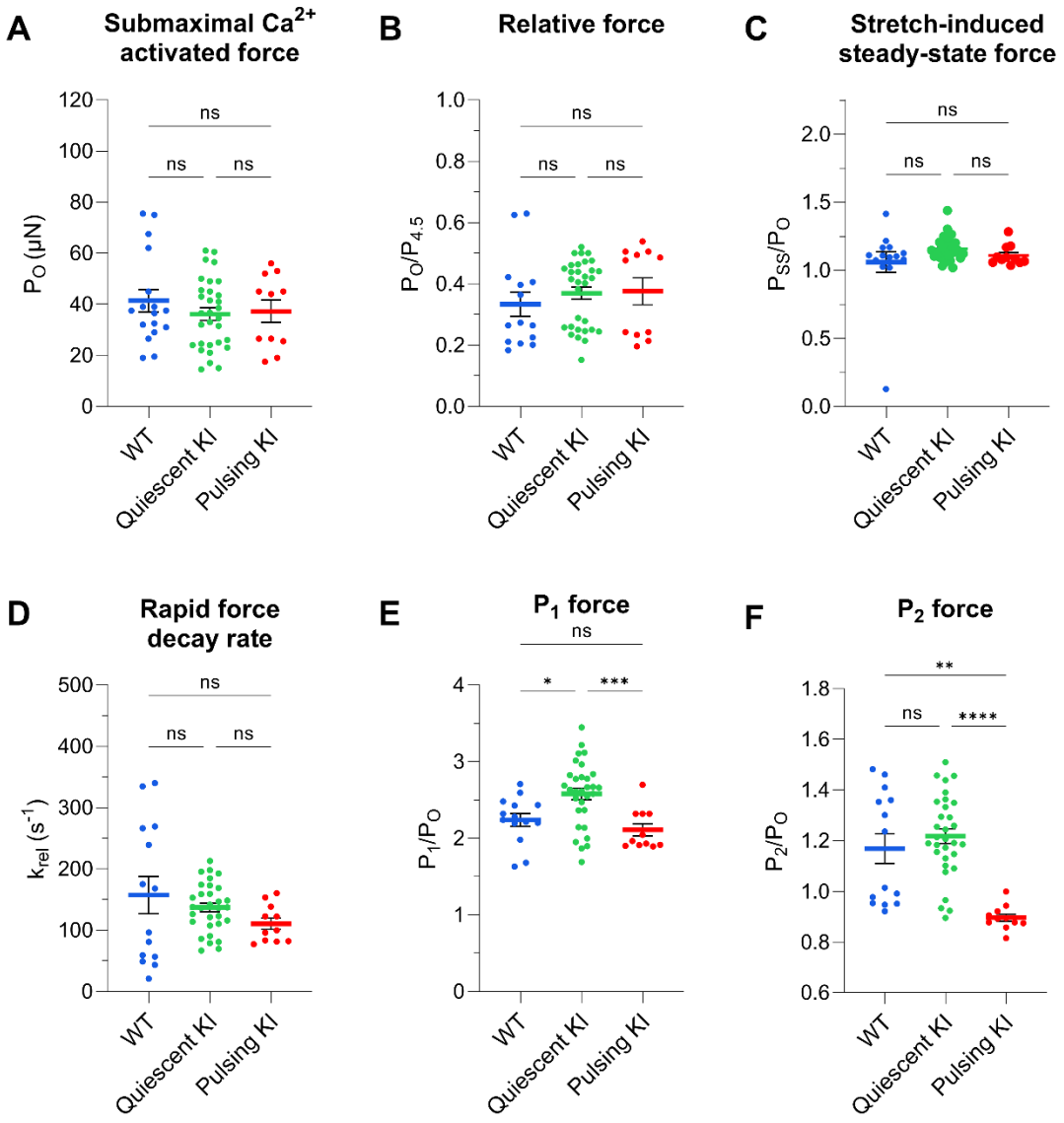

Figure 3. 5 Additional stretch activation properties of fibers undergoing step-stretch protocol. **(A-F)** Stretch activation parameters of fibers *(Figure 3 A-C')* were plotted where each point represents a stretch event. Stretches that did not induce a stretch-activated response (P_{TO}=0) were excluded from final analysis. Submaximal Ca^{2+} activated force reported as absolute force **(A**, P_O**)** and relative to maximal Ca^{2+} activated force **(B**, $P_O/P_{4.5}$**)** were similar among WT, quiescent KI, and pulsing KI fibers. P_{SS}, P1, and P2 were normalized to P_O to allow for comparisons among fibers. Stretch-induced steady-state force **(C**, P_{SS}/P_O**)** and rapid force decay rate (k_{rel}) were comparable among the three fiber populations. Moreover, P_1 force **(E**, P_1/P_O**)** was higher in quiescent KI fibers compared to WT or pulsing KI fibers, and P_2 force **(F**, P_2/P_O**)** was lower in pulsing KI fibers compared to WT or quiescent KI fibers. *n*=14 stretches of *n'*=4 fibers from *n"*=3 WT mice; and *n*=31 stretches of *n'*=7 quiescent KI fibers and *n*=11 stretches of *n'*=3 pulsing KI fibers from *n"*=5 KI mice. Data is presented as mean ± SEM and statistical significance was determined by ordinary one-way ANOVA followed by Tukey's test for multiple comparisons **(A-B)**, or Brown-Forsythe and Welch ANOVA followed by Dunnett's T3 test for multiple comparisons **(C-F)**; ns: not significant, *p<0.05, **p<0.01, ***p<0.001, and ****p<0.0001.

The stretch-activated force (P_{TO}), characterizing the force developed during *phase 3*, was also compared across the three groups. Remarkably, stretch activation in pulsing KI fibers was significantly higher compared to WT and quiescent KI fibers by factors of ~2.6 and ~3.5, respectively **(Figure 3.4 E)**. This pronounced augmentation of stretch activation in pulsing KI fibers is the most conspicuous mechanical property distinguishing pulsing *versus* non-pulsing fibers, suggesting that enhanced stretch activation may qualify pulsatile activity in E248K KI slow-twitch fibers.

3.4 Discussion

The pulsing phenotype we uncovered in a subpopulation of E248K KI fibers is the first to describe a possible underlying mechanism of myogenic tremor. Myotrem is caused by pathogenic polymorphisms in *MYBPC1*, the gene encoding sMyBP-C, which is exclusively expressed in skeletal muscle. Due to the lack of neuropathy in individuals afflicted with Myotrem (14), the characteristic tremor of this myopathy is believed to originate within the muscle itself (14, 24). However, the mechanism eliciting this myogenic tremor has remained elusive. For the first time, we show intrinsic pulsatile activity of permeabilized Myotrem myofibers in the absence of neurological input or stimulation through canonical excitation-contraction coupling. Our prior work on the E248K Myotrem mouse model did not show this behavior in either intact whole muscle or permeabilized fibers from extensor digitorum longus (EDL) muscle (24). Immunoblot analysis revealing that type-I fibers exhibited pulsatile activity may explain why pulses weren't observed in the type-II-dominant EDL. However, because type-I fibers were also present in the

quiescent KI group, a slow fiber type is necessary but likely not sufficient to elicit a pulsatile phenotype in the presence of mutant sMyBP-C.

Quiescent and pulsing KI fibers existing in the same muscle exhibit antithetical responses of stretch activation. While stretch activation developed by quiescent KI fibers is similar to WT, pulsing KI fibers have an enhanced stretch-activated response compared to either group. In addition to fiber type, other factors such as the levels of WT and mutant sMyBP-C or the different combinations and ratios of *Mybpc1* splice variants expressed in each fiber may contribute to the distinct mechanical and stretch activation properties of pulsatile and quiescent fibers. Together these may define the disparate subpopulations of KI fibers and determine pulsatile potential. We posit that the subpopulation of pulsing KI fibers may serve a specialized role as the pacemaker in the generation of the observed myogenic tremor.

Stretch activation is accepted as an essential mechanism contributing to asynchronous IFM contractions, but has also been proposed to play a role in spontaneous oscillatory contraction (SPOC) (70). SPOC is characterized by its saw-tooth pattern of rapid lengthening and slow shortening cycle (64) and contrasts with the regular sinusoidal pattern of contraction and persistence exhibited by pulsing Myotrem fibers. A single case of highly synchronous SPOC has been reported in the literature, observed in permeabilized rabbit psoas fibers in isotonic conditions (71), which mirrors the pulsatile activity we observed in KI fibers in terms of regularity. However, this synchronous SPOC persists on a timescale of only seconds, whereas the pulsatile behavior we describe persists on a timescale of minutes.

While the mechanisms of stretch activation are still unknown, X-ray diffraction studies in IFM propose a model where troponin functions as a bridge between thick and thin filaments, allowing for communication of mechanical strain between the two filaments upon fiber stretch (72, 73). In vertebrate muscles, a similar role could be played by MyBP-C which likewise simultaneously interacts with both thick and thin filaments. The expression levels and phosphorylation of MyBP-C were found to regulate stretch activation in permeabilized cardiac and skeletal muscle fibers (66, 67, 74). Relatedly, MyBP-C has also been shown to regulate SPOC, as removal of its NH_2-terminal region in cardiac myocytes leads to an increase in SPOC (75), prompting a newly proposed role of MyBP-C as a SPOC "wave breaker" (64). Given MyBP-C's essential role in stretch activation, it is conceivable that mutations in *MYBPC1* give rise to pulsatile activity at the fiber level, related to IFM asynchronous contractions and/or SPOC.

Pulsatile activity in KI fibers was dormant in relaxing solution, present in submaximal Ca^{2+} solutions, and absent at maximal Ca^{2+} concentrations. Consequently, Ca^{2+} is required for pulsing, but pulsing behavior is entirely distinct from maximal Ca^{2+} activated contraction. This finding aligns with the fact that the Myotrem tremor is not a resting tremor but induced by posture and action (14, 17). Pulse frequency and amplitude also varied within pulsing fibers in a pCa-dependent manner, as well as among pulsing fibers. This supports the hypothesis of multiple tremor pacemakers in the body, consistent with dual-channel electromyography (EMG) recordings in Myotrem patients revealing temporally asynchronous tremors between the two legs and tremor of incongruent frequency between the two arms (14).

The EMG studies also describe preservation in tremor frequency upon loading, suggesting some degree of central nervous system (CNS) involvement in the observable tremor (14). Accordingly, the muscle spindle and Golgi tendon organ serve as sensory receptors in skeletal muscle, which, upon stretch or compaction due to force generation, send an afferent signal to the CNS (76, 77). In pathological systems such as Myotrem, pulsatile activity of fibers with enhanced stretch activation may affect proprioception, resulting in propagation of a measurable tremor on the organ level via such sensory receptors. Further studies ranging from fiber to organ to the organism level are required to test this hypothesis and decipher the mechanisms of myogenic tremorgenesis.

CHAPTER 4

Discussion and conclusion

4.1 Conclusions and perspectives

These studies provide novel insights into the role of *MYBPC1* mutations in Myotrem. Because of the rarity of this disease, much is still unknown about its progression as well as the molecular mechanisms underlying pathogenesis. Using the *MYBPC1* E248K murine model, we characterized contractile function in mid- and late-adulthood and found that the stabilization that occurs in mid-life expires in late adulthood. This leads to a loss of native muscle structure and function in a sex-specific manner. These studies highlight the need for early intervention to prevent the effects of this decline and/or the development of effective therapeutic options for afflicted individuals. The sex-dependent nature of disease progression, whereby males are more affected than females, suggest a role of sex hormones such as estrogen that potentially modifies disease phenotype and delays the onset of age-related degeneration.

These studies explicitly describe an inverse relationship between contractile function and sarcomeric order. The quantitative method of measuring sarcomeric (dis)order we developed could potentially be applied to other tissues to predict contractile function. For example, as new genetic variants of unknown significance are identified, this method could be used to quantify sarcomeric organization and predict myopathic severity. These studies also further establish sMyBP-C's role as a structural protein (6, 7), that links sarcomeric disorganization as an underlying mechanism for muscle weakness in Myotrem tissues.

In addition to muscle weakness, we also investigate a putative mechanism for myogenic tremorgenesis and uncovered a subpopulation of slow-twitch fibers isolated from KI soleus that exhibited autonomous regular pulsatile activity in submaximal Ca^{2+} conditions. This pulsative activity resembles spontaneous oscillatory contractions (64) with a distinguishing high level of regularity and persistence. The fibers showing this activity exhibited enhanced stretch activation properties, similar to insect indirect flight muscle (60), which is likely to give rise to this pulse activity. As they only constitute a small percentage of fibers in the soleus, we posit that these fibers function as the pacemaker of myogenic tremor, supporting the hypothesis of a new entity of tremor originating in the muscle itself. Although further studies are required to fully understand myogenic tremorgenesis, these studies provide insight into its possible mechanism.

Furthermore, the role of only a subpopulation of myofibers displaying pulse activity gives rise to an additional axis in which to describe subpopulations of fibers within a single muscle pathogenic tissue. In addition to conspicuous aspects such as fiber type, differences in stretch-activation properties give to a discrete subpopulation of fibers with the potential to display pulse activity in the presence of the E248K mutation. Because these fiber subpopulations often display antithetical properties, these characteristic differences may be overlooked if analyzed as one pooled population. This highlights the complexity of skeletal tissue even on the level of specific tissues and may provide evidence for the need for future studies characterizing Myotrem fibers to be performed on the single fiber level.

4.2 Future directions

Our studies have advanced our understanding of the role of sMyBP-C in Myotrem by highlighting its role in maintaining sarcomeric and myofibrillar structure, carried out in fixed sections of muscle. However, these studies are limited in resolution and their static nature. Super-resolution microscopy and/or electron microscopy would allow for higher resolution and structural analysis on the ultrastructural and molecular levels. Furthermore, advancements in small angle x-ray diffraction (XRD) techniques allow more comprehensive and less biased structural analysis of myofibers (78). These studies can also be performed on permeabilized fibers in a gradient of Ca^{2+} conditions to understand how calcium may affect structure during relaxation and contraction. These studies may give greater insight into the structural alterations and provide insight into how fiber subpopulations, original tissues, sex, and age could affect myofiber structure and function.

On the biochemical and molecular levels, sMyBP-C undergoes extensive alternative splicing as well as phosphorylation, which are implicated in disease (10, 11). The effects of these events on sMyBP-C have yet to be tested in Myotrem in the presence of the E248K mutation. Phosphorylation and splice variant profiles can determined using phosphate affinity electrophoresis and tandem immunoblotting with phosho-specific antibodies, much like studies performed by Ackermann *et al (10, 11).* These studies could then be followed by binding studies and *in vitro* gliding assays with recombinant protein to determine the combined effect of splice variant, phosphorylation, and presence or absence of the Myotrem mutation to determine how these factors would affect sMyBP-C function. These biochemical assays would provide greater insight into the molecular and biochemical effects of Myotrem.

It should be noted that, although it has provided a powerful tool for *in vivo* characterization, the *MYBPC1* E248K mouse model only harbors one of the five described Myotrem mutations. *In vitro* binding studies have uncovered unique and sometimes antithetical perturbations amongst the Myotrem mutations. For example, the E248K and the L263R mutations show opposite trends in binding to heavy meromyosin (HMM) (14, 15). This begets the question of how different mutations can cause different molecular effects yet lead to the same or a similar myopathy. Here, an investigation into mutation-specific effects from the molecular to the whole-organism levels would be of interest. Subsequent characterization in both similarities and differences would be important in understanding Myotrem pathogenesis and how it might explain differences in manifestation in individuals afflicted with Myotrem.

Finally, one of the main goals for studying Myotrem beyond understanding sMyBP-C biology and pathology is the need for development of effective therapeutics. Tremor and muscle weakness often affect quality of life. Furthermore, our studies with the E248K murine model predict a sharp decline in muscle function in late adulthood. Because of its autosomal dominant pattern of inheritance, half of all offspring with an affected parent inherit the pathogenic polymorphism and myopathic phenotype. A deeper understanding of altered binding and aberrant contractile behavior will help inform disease development. For example, a small molecule that restores binding to resemble WT and/or a targeted therapy that targets the pacemaker function of pulsing cells may be viable options to explore. Although much has been accomplished in the understanding of sMyBP-C, more effort is required to apply this knowledge to patients and to provide effective therapeutic options for individuals with Myotrem.

REFERENCES

1. Ackermann MA, Kontrogianni-Konstantopoulos A. Myosin binding protein-C slow: an intricate subfamily of proteins. J Biomed Biotechnol. 2010;2010:652065.

2. Wang L, Geist J, Grogan A, Hu LR, Kontrogianni-Konstantopoulos A. Thick Filament Protein Network, Functions, and Disease Association. Compr Physiol. 2018;8(2):631-709.

3. Heling L, Geeves MA, Kad NM. MyBP-C: one protein to govern them all. J Muscle Res Cell Motil. 2020;41(1):91-101.

4. Harris SP, Lyons RG, Bezold KL. In the thick of it: HCM-causing mutations in myosin binding proteins of the thick filament. Circ Res. 2011;108(6):751-64.

5. Geist J, Kontrogianni-Konstantopoulos A. MYBPC1, an Emerging Myopathic Gene: What We Know and What We Need to Learn. Front Physiol. 2016;7:410.

6. Geist J, Ward CW, Kontrogianni-Konstantopoulos A. Structure before function: myosin binding protein-C slow is a structural protein with regulatory properties. FASEB J. 2018;32(12):fj201800624R.

7. Song T, McNamara JW, Baby A, Ma W, Landim-Vieira M, Natesan S, et al. Unlocking the Role of sMyBP-C: A Key Player in Skeletal Muscle Development and Growth. bioRxiv. 2023.

8. Ackermann MA, Kontrogianni-Konstantopoulos A. Myosin binding protein-C slow is a novel substrate for protein kinase A (PKA) and C (PKC) in skeletal muscle. J Proteome Res. 2011;10(10):4547-55.

9. Ackermann MA, Kontrogianni-Konstantopoulos A. Myosin binding protein-C slow: a multifaceted family of proteins with a complex expression profile in fast and slow twitch skeletal muscles. Front Physiol. 2013;4:391.

10. Ackermann MA, Ward CW, Gurnett C, Kontrogianni-Konstantopoulos A. Myosin Binding Protein-C Slow Phosphorylation is Altered in Duchenne Dystrophy and Arthrogryposis Myopathy in Fast-Twitch Skeletal Muscles. Sci Rep. 2015;5:13235.

11. Ackermann MA, Kerr JP, King B, C WW, Kontrogianni-Konstantopoulos A. The Phosphorylation Profile of Myosin Binding Protein-C Slow is Dynamically Regulated in Slow-Twitch Muscles in Health and Disease. Sci Rep. 2015;5:12637.

12. Gurnett CA, Desruisseau DM, McCall K, Choi R, Meyer ZI, Talerico M, et al. Myosin binding protein C1: a novel gene for autosomal dominant distal arthrogryposis type 1. Hum Mol Genet. 2010;19(7):1165-73.

13. Markus B, Narkis G, Landau D, Birk RZ, Cohen I, Birk OS. Autosomal recessive lethal congenital contractural syndrome type 4 (LCCS4) caused by a mutation in MYBPC1. Hum Mutat. 2012;33(10):1435-8.

14. Stavusis J, Lace B, Schafer J, Geist J, Inashkina I, Kidere D, et al. Novel mutations in MYBPC1 are associated with myogenic tremor and mild myopathy. Ann Neurol. 2019;86(1):129-42.

15. Shashi V, Geist J, Lee Y, Yoo Y, Shin U, Schoch K, et al. Heterozygous variants in MYBPC1 are associated with an expanded neuromuscular phenotype beyond arthrogryposis. Hum Mutat. 2019;40(8):1115-26.

16. Stavusis J, Geist J, Kontrogianni-Konstantopoulos A. Sarcomeric myopathies associated with tremor: new insights and perspectives. J Muscle Res Cell Motil. 2020;41(4):285-95.

17. Schaefer J, Saak A, Bonnemann CG, Jackson S. Myogenic tremor - a novel tremor entity. Curr Opin Neurol. 2021;34(5):706-13.

18. Uneoka S, Kobayashi T, Numata-Uematsu Y, Oikawa Y, Katata Y, Okubo Y, et al. A Case Series of Patients With MYBPC1 Gene Variants Featuring Undulating Tongue Movements as Myogenic Tremor. Pediatr Neurol. 2023;146:16-20.

19. Shiraishi K, Tsuburaya RS, Mukaida S, Yano N, Yoshida T. A case of congenital myopathy accompanied by tremor due to a MYBPC1 mutation. Pediatr Int. 2022;64(1):e15061.

20. Zhao Y, Yan C, Ji K. Ultrasonography of Muscle Vibration Caused by MYBPC1 Variant. JAMA Neurol. 2023;80(7):757.

21. Leduc-Pessah H, Smith IC, Kernohan KD, Sampaio M, Melkus G, Strasser L, et al. Congenital tremor and myopathy secondary to novel MYBPC1 variant. J Neurol Sci. 2024;457:122864.

22. Kulikovskaya I, McClellan G, Flavigny J, Carrier L, Winegrad S. Effect of MyBP-C binding to actin on contractility in heart muscle. J Gen Physiol. 2003;122(6):761-74.

23. Gruen M, Prinz H, Gautel M. cAPK-phosphorylation controls the interaction of the regulatory domain of cardiac myosin binding protein C with myosin-S2 in an on-off fashion. FEBS Lett. 1999;453(3):254-9.

24. Geist Hauserman J, Stavusis J, Joca HC, Robinett JC, Hanft L, Vandermeulen J, et al. Sarcomeric deficits underlie MYBPC1-associated myopathy with myogenic tremor. JCI Insight. 2021;6(19).

25. Howarth JW, Ramisetti S, Nolan K, Sadayappan S, Rosevear PR. Structural insight into unique cardiac myosin-binding protein-C motif: a partially folded domain. J Biol Chem. 2012;287(11):8254-62.

26. Gorcenco S, Ilinca A, Almasoudi W, Kafantari E, Lindgren AG, Puschmann A. New generation genetic testing entering the clinic. Parkinsonism Relat Disord. 2020;73:72-84.

27. Lyons KE, Pahwa R, Comella CL, Eisa MS, Elble RJ, Fahn S, et al. Benefits and risks of pharmacological treatments for essential tremor. Drug Saf. 2003;26(7):461-81.

28. Iyer A, Lauerova B, Mariano J, Haberlova J, Lassuthova P, Zidkova J, et al. Compound heterozygous variants in MYBPC1 lead to severe distal arthrogryposis type-1 manifestations. Gene. 2024;910:148339.

29. Geist J, Ward CW, Kontrogianni-Konstantopoulos A. Structure before function: myosin binding protein-C slow is a structural protein with regulatory properties. FASEB J. 2018:fj201800624R.

30. Ackermann MA, Kontrogianni-Konstantopoulos A. Myosin binding protein-C: a regulator of actomyosin interaction in striated muscle. J Biomed Biotechnol. 2011;2011:636403.

31. Ackermann MA, Hu LY, Bowman AL, Bloch RJ, Kontrogianni-Konstantopoulos A. Obscurin interacts with a novel isoform of MyBP-C slow at the periphery of the sarcomeric M-band and regulates thick filament assembly. Mol Biol Cell. 2009;20(12):2963-78.

32. Weber FE, Vaughan KT, Reinach FC, Fischman DA. Complete sequence of human fast-type and slow-type muscle myosin-binding-protein C (MyBP-C). Differential expression, conserved domain structure and chromosome assignment. Eur J Biochem. 1993;216(2):661-9.

33. Dutta S, Sengupta P. Men and mice: Relating their ages. Life Sci. 2016;152:244-8.

34. McNamara JW, Li A, Dos Remedios CG, Cooke R. The role of super-relaxed myosin in skeletal and cardiac muscle. Biophys Rev. 2015;7(1):5-14.

35. McNamara JW, Li A, Smith NJ, Lal S, Graham RM, Kooiker KB, et al. Ablation of cardiac myosin binding protein-C disrupts the super-relaxed state of myosin in murine cardiomyocytes. J Mol Cell Cardiol. 2016;94:65-71.

36. McNamara JW, Sadayappan S. Skeletal myosin binding protein-C: An increasingly important regulator of striated muscle physiology. Arch Biochem Biophys. 2018;660:121-8.

37. Bigland-Ritchie B, Woods JJ. Changes in muscle contractile properties and neural control during human muscular fatigue. Muscle Nerve. 1984;7(9):691-9.

38. Bigland-Ritchie B, Thomas CK, Rice CL, Howarth JV, Woods JJ. Muscle temperature, contractile speed, and motoneuron firing rates during human voluntary contractions. J Appl Physiol (1985). 1992;73(6):2457-61.

39. MacIntosh BR, Willis JC. Force-frequency relationship and potentiation in mammalian skeletal muscle. J Appl Physiol (1985). 2000;88(6):2088-96.

40. Li X, Zhong B, Han W, Zhao N, Liu W, Sui Y, et al. Two novel mutations in myosin binding protein C slow causing distal arthrogryposis type 2 in two large Han Chinese families may suggest important functional role of immunoglobulin domain C2. PLoS One. 2015;10(2):e0117158.

41. Degens H, Korhonen MT. Factors contributing to the variability in muscle ageing. Maturitas. 2012;73(3):197-201.

42. Toepfer CN, Garfinkel AC, Venturini G, Wakimoto H, Repetti G, Alamo L, et al. Myosin Sequestration Regulates Sarcomere Function, Cardiomyocyte Energetics, and Metabolism, Informing the Pathogenesis of Hypertrophic Cardiomyopathy. Circulation. 2020;141(10):828-42.

43. Ranu N, Laitila J, Dugdale HF, Mariano J, Kolb JS, Wallgren-Pettersson C, et al. NEB mutations disrupt the super-relaxed state of myosin and remodel the muscle metabolic proteome in nemaline myopathy. Acta Neuropathol Commun. 2022;10(1):185.

44. Narici M, McPhee J, Conte M, Franchi MV, Mitchell K, Tagliaferri S, et al. Age-related alterations in muscle architecture are a signature of sarcopenia: the ultrasound sarcopenia index. J Cachexia Sarcopenia Muscle. 2021;12(4):973-82.

45. Enns DL, Tiidus PM. Estrogen influences satellite cell activation and proliferation following downhill running in rats. J Appl Physiol (1985). 2008;104(2):347-53.

46. Colson BA, Petersen KJ, Collins BC, Lowe DA, Thomas DD. The myosin super-relaxed state is disrupted by estradiol deficiency. Biochem Biophys Res Commun. 2015;456(1):151-5.

47. Phung LA, Karvinen SM, Colson BA, Thomas DD, Lowe DA. Age affects myosin relaxation states in skeletal muscle fibers of female but not male mice. PLoS One. 2018;13(9):e0199062.

48. Rosa-Caldwell ME, Greene NP. Muscle metabolism and atrophy: let's talk about sex. Biol Sex Differ. 2019;10(1):43.

49. Sipila S, Narici M, Kjaer M, Pollanen E, Atkinson RA, Hansen M, et al. Sex hormones and skeletal muscle weakness. Biogerontology. 2013;14(3):231-45.

50. Greising SM, Baltgalvis KA, Lowe DA, Warren GL. Hormone therapy and skeletal muscle strength: a meta-analysis. J Gerontol A Biol Sci Med Sci. 2009;64(10):1071-81.

51. Velders M, Schleipen B, Fritzemeier KH, Zierau O, Diel P. Selective estrogen receptor-beta activation stimulates skeletal muscle growth and regeneration. FASEB J. 2012;26(5):1909-20.

52. Fragala MS, Kenny AM, Kuchel GA. Muscle quality in aging: a multi-dimensional approach to muscle functioning with applications for treatment. Sports Med. 2015;45(5):641-58.

53. Christensen K, Doblhammer G, Rau R, Vaupel JW. Ageing populations: the challenges ahead. Lancet. 2009;374(9696):1196-208.

54. Laws N, Hoey A. Progression of kyphosis in mdx mice. J Appl Physiol (1985). 2004;97(5):1970-7.

55. Wei S, Guo A, Chen B, Kutschke W, Xie YP, Zimmerman K, et al. T-tubule remodeling during transition from hypertrophy to heart failure. Circ Res. 2010;107(4):520-31.

56. Craig R, Offer G. The location of C-protein in rabbit skeletal muscle. Proc R Soc Lond B Biol Sci. 1976;192(1109):451-61.

57. Okagaki T, Weber FE, Fischman DA, Vaughan KT, Mikawa T, Reinach FC. The major myosin-binding domain of skeletal muscle MyBP-C (C protein) resides in the COOH-terminal, immunoglobulin C2 motif. J Cell Biol. 1993;123(3):619-26.

58. Moos C. Fluorescence microscope study of the binding of added C protein to skeletal muscle myofibrils. J Cell Biol. 1981;90(1):25-31.

59. Campbell KB, Chandra M. Functions of stretch activation in heart muscle. J Gen Physiol. 2006;127(2):89-94.

60. Linari M, Reedy MK, Reedy MC, Lombardi V, Piazzesi G. Ca-activation and stretch-activation in insect flight muscle. Biophys J. 2004;87(2):1101-11.

61. Pringle JW. The excitation and contraction of the flight muscles of insects. J Physiol. 1949;108(2):226-32.

62. Cao T, Jin JP. Evolution of Flight Muscle Contractility and Energetic Efficiency. Front Physiol. 2020;11:1038.

63. Josephson RK, Malamud JG, Stokes DR. Asynchronous muscle: a primer. J Exp Biol. 2000;203(Pt 18):2713-22.

64. Harris SP. Making waves: A proposed new role for myosin-binding protein C in regulating oscillatory contractions in vertebrate striated muscle. J Gen Physiol. 2021;153(3).

65. Stelzer JE, Moss RL. Contributions of stretch activation to length-dependent contraction in murine myocardium. J Gen Physiol. 2006;128(4):461-71.

66. Stelzer JE, Dunning SB, Moss RL. Ablation of cardiac myosin-binding protein-C accelerates stretch activation in murine skinned myocardium. Circ Res. 2006;98(9):1212-8.

67. Robinett JC, Hanft LM, Biesiadecki B, McDonald KS. Molecular regulation of stretch activation. Am J Physiol Cell Physiol. 2022;323(6):C1728-C39.

68. Vinciguerra C, Iacono S, Bevilacqua L, Landolfi A, Piscosquito G, Ginanneschi F, et al. Sex differences in neuromuscular disorders. Mech Ageing Dev. 2023;211:111793.

69. Hinken AC, McDonald KS. Inorganic phosphate speeds loaded shortening in rat skinned cardiac myocytes. Am J Physiol Cell Physiol. 2004;287(2):C500-7.

70. Smith DA, Stephenson DG. The mechanism of spontaneous oscillatory contractions in skeletal muscle. Biophys J. 2009;96(9):3682-91.

71. Yasuda K, Shindo Y, Ishiwata S. Synchronous behavior of spontaneous oscillations of sarcomeres in skeletal myofibrils under isotonic conditions. Biophys J. 1996;70(4):1823-9.

72. Perz-Edwards RJ, Irving TC, Baumann BA, Gore D, Hutchinson DC, Krzic U, et al. X-ray diffraction evidence for myosin-troponin connections and tropomyosin movement during stretch activation of insect flight muscle. Proc Natl Acad Sci U S A. 2011;108(1):120-5.

73. Bullard B, Pastore A. Regulating the contraction of insect flight muscle. J Muscle Res Cell Motil. 2011;32(4-5):303-13.

74. Stelzer JE, Patel JR, Moss RL. Protein kinase A-mediated acceleration of the stretch activation response in murine skinned myocardium is eliminated by ablation of cMyBP-C. Circ Res. 2006;99(8):884-90.

75. Napierski NC, Granger K, Langlais PR, Moran HR, Strom J, Touma K, et al. A Novel "Cut and Paste" Method for In Situ Replacement of cMyBP-C Reveals a New Role for cMyBP-C in the Regulation of Contractile Oscillations. Circ Res. 2020;126(6):737-49.

76. Proske U, Gandevia SC. The proprioceptive senses: their roles in signaling body shape, body position and movement, and muscle force. Physiol Rev. 2012;92(4):1651-97.

77. Kistemaker DA, Van Soest AJ, Wong JD, Kurtzer I, Gribble PL. Control of position and movement is simplified by combined muscle spindle and Golgi tendon organ feedback. J Neurophysiol. 2013;109(4):1126-39.

78. Ma W, Irving TC. Small Angle X-ray Diffraction as a Tool for Structural Characterization of Muscle Disease. Int J Mol Sci. 2022;23(6).